J. Fluid Mech. (2022), *vol*. 949, A7, doi:10.1017/jfm.2022.731

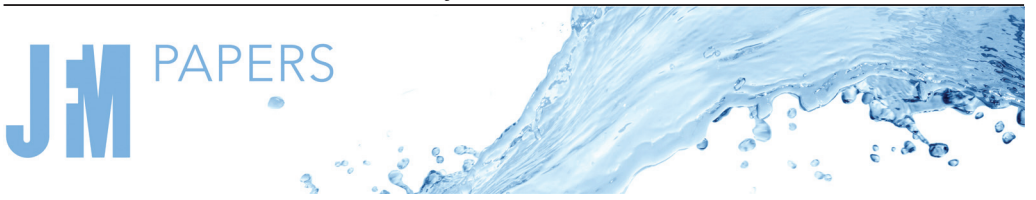

Modelling the downstream development of a turbulent boundary layer following a step change of roughness

Mogeng Li[1,2], Charitha M. de Silva[2,3], Daniel Chung[2], Dale I. Pullin[4], Ivan Marusic[2] and Nicholas Hutchins[2,†]

[1]Physics of Fluids Group, Max Planck Center for Complex Fluid Dynamics, J.M. Burgers Center for Fluid Dynamics, Department of Science and Technology, University of Twente, 7500AE Enschede, The Netherlands

[2]Department of Mechanical Engineering, University of Melbourne, Victoria 3010, Australia

[3]School of Mechanical and Manufacturing Engineering, University of New South Wales, NSW 2052, Australia

[4]Graduate Aerospace Laboratories, California Institute of Technology, CA 91125, USA

(Received 29 May 2022; revised 2 August 2022; accepted 19 August 2022)

In this study, we develop an analytical model to predict the turbulent boundary layer downstream of a step-change in the surface roughness where upstream flow conditions are given. We first revisit the classical model of Elliott (*Trans. Am. Geophys. Union*, vol. 39, 1958, pp. 1048–1054), who modelled the velocity distribution within and above the internal layer with a simple piecewise logarithmic profile, and evolved the velocity profile using the streamwise momentum equation. Elliott's model was originally developed for an atmospheric surface layer, and to make the model applicable to a spatially developing turbulent boundary layer with finite thickness, we propose a number of more physical refinements, including adding a wake function to the velocity profile, considering the growth of the entire boundary layer in the streamwise direction, and using a more realistic shear stress profile in the momentum equation. In particular, we implement the blending model (Li *et al.*, *J. Fluid Mech.*, vol. 923, 2021, p. A18) to account for the deviation of the mean flow within the internal layer from a canonical velocity profile based on the local wall condition. These refinements lead to improved agreement between the prediction and the measurement, especially in the vicinity of the rough-to-smooth change.

Key words: turbulent boundary layers

† Email address for correspondence: nhu@unimelb.edu.au

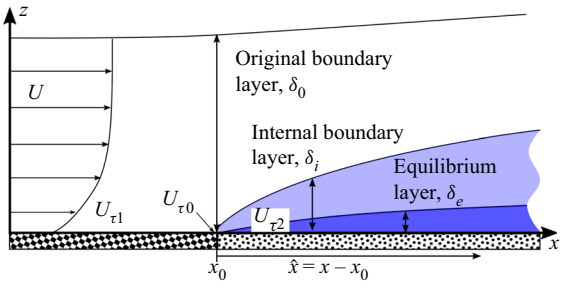

Figure 1. Schematic of a turbulent boundary layer over a step change in surface roughness condition. The roughness transition occurs at x_0, and $\hat{x} = x - x_0$ denotes the fetch downstream of the transition.

1. Introduction

A turbulent boundary layer over a streamwise change in wall roughness can be considered to be a distillation of flows commonly observed in nature and industry, examples of which include a surface layer where a forest terrain changes to a prairie, and a turbulent boundary layer developing on a ship's hull with patchy biofouling. Understanding the behaviour of the flow downstream of a step-change in roughness and the ability to model the flow evolution are beneficial to atmospheric forecasting, as well as drag estimation for better fuel efficiency.

A schematic of the flow configuration is shown in figure 1. A turbulent boundary layer develops on a wall, the roughness of which abruptly changes at $x = x_0$. Here, x represents the streamwise direction and z represents the wall-normal direction. The fetch on the downstream surface is then denoted as $\hat{x} = x - x_0$. The flow adapts to the new wall condition firstly close to the wall, and the affected region (light blue shaded region) widens farther downstream. This region, where the flow is modified by the new wall condition, is usually referred to as the internal layer or internal boundary layer (IBL), and its thickness is denoted by δ_i. The topic has been reviewed by Garratt (1990), and the application in meteorology has recently been reviewed by Bou-Zeid *et al.* (2020). The flow structures with characteristics of the upstream roughness are considered to persist above the IBL. An equilibrium layer (EL) can also be defined as the near-wall region where the flow has fully adapted to the new surface condition, and its thickness is denoted by δ_e. Traditionally, δ_e has been assessed by comparing the mean streamwise velocity profile or shear stress profile scaled by the local friction velocity with the corresponding profile of the downstream surface (Rao, Wyngaard & Coté 1974). In this study, we define both IBL and EL using the mean velocity profile.

Predicting the evolution of the flow downstream of a roughness step change, given the surface and upstream flow conditions, has attracted great interest in the past few decades. It has important applications in the site selection of a meteorology measurement tower, where it is desirable to choose a location at a sufficient distance away from the change in surface condition to avoid the 'leading-edge effects'. The tower should also be submerged in the EL in order to sample the quantities associated with the local wall condition rather than the remnant of upstream structures. A detailed summary of various modelling attempts can be found in the work by Savelyev & Taylor (2005). A crude rule of thumb to estimate the IBL thickness is $\delta_i/\hat{x} \approx 1/10$ and $\delta_e/\hat{x} \approx 1/200$ (Rao *et al.* 1974). Power-law relationships with a form of $\delta_i \propto \hat{x}^{\alpha}$ are obtained by empirically fitting to experimentally or numerically generated data, and the exponent varies from 0.2 to 1 across studies (Rouhi, Chung & Hutchins 2019). Although these relationships are easy to

implement, they are usually obtained from a particular set of surface and flow conditions and cannot be generalised to others.

There are considerable attempts in the literature to theoretically model the flow response to a step change in the wall condition, and they can be classified into two major categories based on the assumptions made. Most of these models are developed in the context of atmospheric surface layers where the canonical mean velocity profile can be approximated by a log-law. The first category of theoretical models is established on the diffusion analogy, which was introduced by Miyake (1965). In this approach, the IBL is assumed to propagate in the same manner as a passive contaminant, and the growth rate of δ_i is proportional to $w_{rms}(\delta_i) = (\overline{w^2})^{1/2}$, the vertical diffusion intensity at the interface. That is,

$$\frac{\mathrm{d}\delta_i}{\mathrm{d}t} = Aw_{rms}, \tag{1.1}$$

where A is a constant and $\mathrm{d}(\,\cdot\,)/\mathrm{d}(\,\cdot\,)$ denotes the total derivative. Using the chain rule, the left-hand side of the equation can be rewritten as $\mathrm{d}\delta_i/\mathrm{d}t = (\partial\delta_i/\partial x)(\mathrm{d}x/\mathrm{d}t)$ for a steady state ($\partial\delta_i/\partial t = 0$). Assuming $\mathrm{d}x/\mathrm{d}t = U(\delta_i)$, which is the mean velocity at the interface, the equation above can be rewritten as

$$U(\delta_i)\frac{\mathrm{d}\delta_i}{\mathrm{d}x} = Aw_{rms}. \tag{1.2}$$

After relating the w_{rms} term to the friction velocity (upstream or downstream) through an assumed proportionality in neutrally stratified flow, $w_{rms} = CU_\tau$ (C is also a constant), determining the velocity at the interface $U(\delta_i)$ from a logarithmic profile and prescribing an initial condition of $\delta_i|_{\hat{x}=0}$, (1.2) can be integrated to obtain the final expression of the IBL growth. Models with various expressions of the w_{rms} and $U(\delta_i)$ terms were developed (Jackson 1976; Panofsky & Dutton 1984; Savelyev & Taylor 2001; Bou-Zeid, Meneveau & Parlange 2004; Yang 2016), and it was also extended to non-neutral stability conditions (Savelyev & Taylor 2005).

A second group of models assume a form of the recovering mean velocity profile, and then relate the local wall-shear stress to the growth of the IBL through the streamwise momentum equation. This approach was established in the seminal study of Elliott (1958), where a piecewise logarithmic velocity profile with a change in slope across the edge of the IBL was used. Shear stress, as derived from the slope of the log-law profile through a 'mixing-length' relation, takes the form of a step function, and attempts were made to eliminate the discontinuity at the edge of the IBL by using a velocity profile integrated from a shear-stress profile that linearly changes from the downstream value to the upstream one across the IBL (Panofsky & Townsend 1964). So far in both mean velocity profile models described, the flow above the IBL remains unmodified from that upstream of the step change and no streamwise development of the flow in this region is considered. That is to say, if we denote the upstream velocity profile as $U_1(z)$ (where z is the wall-normal position), then $U(z) = U_1(z)$ will hold for all $z > \delta_i$. Another way of modelling the flow is to assume that the mean velocity remains constant along a streamline above the IBL, while within the IBL the acceleration of the mean velocity along the same streamline is self-similar (Townsend 1965*a*,*b*, 1966). The mean velocity profiles constructed by Elliott (1958) and Panofsky & Townsend (1964) can be incorporated into the Townsend self-similar framework with streamline displacement.

More recently, it has been recognised that the flow in the IBL has not fully adapted to the local wall condition, questioning the applicability of an equilibrium log-law profile, as well as the corresponding mixing-length relation (Antonia & Luxton 1972; Shir 1972;

Rao *et al.* 1974; Ismail, Zaki & Durbin 2018; Rouhi *et al.* 2019). Chamorro & Porté-Agel (2009) proposed a semiempirical blending model of the recovering mean velocity profile without further incorporating the streamwise evolution. They considered that after a rough-to-smooth transition, the mean velocity profile asymptotes to the new smooth-wall log law at the wall and the upstream rough-wall log law at the edge of the IBL. These two limiting cases are then blended by a log-linear weight function, representing the gradual transition from the local smooth-wall log law to the upstream rough-wall counterpart as z/δ_i increases. This model of the velocity profile does not assume a constant or linear distribution of the shear stress in the IBL (as did Elliott (1958) and Panofsky & Townsend (1964)). The agreement with measurements in the near-wall region is further improved by prescribing a finite thickness of the EL (Abkar & Porté-Agel 2012; Ghaisas 2020), or using a log-normal blending function that gives more weight to the smooth-wall profile close to the wall (Li *et al.* 2021).

In addition to the two major categories as discussed above, there have also been other attempts in modelling the flow response to a roughness change. Wood (1982) developed a simple correlation for the IBL thickness from dimensional analysis. Peterson (1969) adopted a closure of the turbulent shear stress and solved the continuity, momentum and turbulent-energy equations numerically. Van Buren *et al.* (2020) performed a perturbation analysis on the mean-momentum equation and Reynolds stress transport equation of a rough-to-smooth change in a pipe flow, and successfully captured the second-order response in the experimental data.

To summarise, Elliott's original model was formulated for an atmospheric surface layer with no consideration of the gradual adjustment of the flow in the IBL to the new wall condition. In this study, we incorporate modifications that make Elliott's approach valid for a turbulent boundary layer with finite thickness. The inherent difference between the current model and Elliott's original formulation is that we consider a finite thickness of the total boundary layer, and introduce an additional momentum equation to describe its spatial growth. The new model is useful for a wide range of engineering applications where a finite-thickness boundary layer is concerned, such as the flow over patches of biofouling roughness on a ship's hull. A series of refinements will be discussed, including reassessing the assumptions originally made concerning a deep surface layer where δ_i/δ_{99} is small, as well as incorporating the blending velocity profile as detailed in Li *et al.* (2021).

The streamwise, spanwise and wall-normal directions are represented by x, y and z. The corresponding time-averaged and fluctuation velocity components are denoted by U, V, W and u, v, w, respectively. Quantities upstream and downstream of the rough-to-smooth transition are distinguished by a subscript $(\cdot)_1$ and $(\cdot)_2$, respectively, and the subscript $(\cdot)_0$ represents quantities at the roughness transition ($x = x_0$ or just prior to it if there is a jump of that quantity across the roughness transition, see figure 1).

This paper is structured as follows. First, Elliott's original model is summarised in § 2, and its numerical implementation is presented in § 3. The model is then evaluated utilising an experimental dataset covering a wide range of flow parameters (Li *et al.* 2021) in § 3.1. Refinements including considering a wake profile, the streamwise growth of the entire boundary layer, a z-dependent shear stress profile, and the blending velocity profile in the IBL (as discussed in Li *et al.* (2021)), are added and compared with the original model in § 4. The performance of the new model is assessed in § 5.

2. A brief review of Elliott's model

In the seminal study of Elliott (1958), a theoretical model predicting the flow recovery from a step change in the surface roughness was established. The flow condition is illustrated

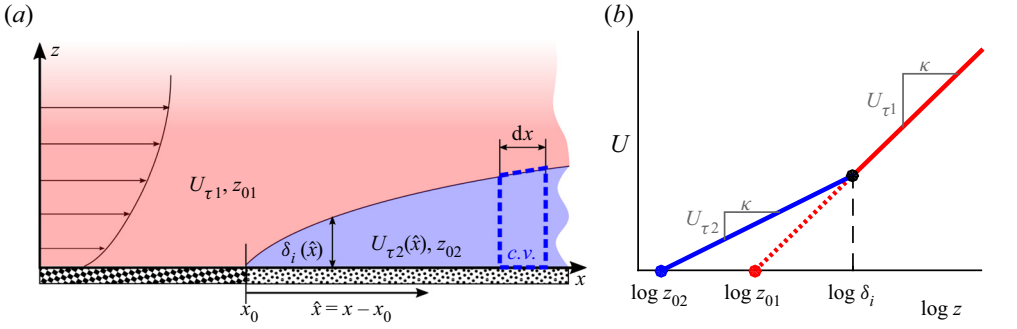

Figure 2. (*a*) Sketch of the flow over a roughness change in the streamwise direction. The IBL is shown by blue, and the outer layer is shown by red. The control volume used to obtain (2.5) is bounded by the dashed line. (*b*) Sketch of the mean velocity profile in Elliott's model corresponding to the flow condition in (*a*). The local inner log-law profile is shown by blue, and the outer log-law profile is shown by red, and a rough-to-smooth transition ($z_{01} > z_{02}$) is assumed in the plot.

in figure 2(*a*). The incoming flow can be fully described by the roughness length z_{01} and friction velocity $U_{\tau 1}$ of the upstream surface, while the only information about the downstream surface is the roughness length z_{02}. Both upstream and downstream surfaces are assumed to be in the fully rough regime, and the roughness length can be related to the equivalent sand grain roughness k_s by

$$z_0 = k_s \exp(-\kappa A'_{fr}), \tag{2.1}$$

where $A'_{fr} = 8.5$ is the fully rough intercept for sand grain roughness (Nikuradse 1950). An extension of the model is to consider that either the upstream or downstream surface is fully smooth, and the roughness length will then be related to the viscous wall unit through

$$z_0 = \frac{\nu}{U_\tau} \exp(-\kappa B), \tag{2.2}$$

where B is the smooth-wall intercept, U_τ is the local friction velocity and ν is the kinematic viscosity of air. Here, the constant values are chosen as $\kappa = 0.384$, $B = 4.17$ (Chauhan, Monkewitz & Nagib 2009). In the scenario of a rough-to-smooth transition, the downstream roughness length z_{02} is directly related to the local friction velocity, which can vary significantly with $\hat{x}$, particularly for $\hat{x}/\delta_0 \lesssim 2$ (Li *et al.* 2021).

After the roughness transition at $x = x_0$ (i.e. $\hat{x} = 0$), an IBL containing the modified flow develops on the downstream surface and a local friction velocity $U_{\tau 2}$ evolves with the growth of the IBL. In this system, the roughness lengths z_{01} and z_{02} are known. Here, $U_{\tau 1}$ is also given and assumed to be constant, therefore, we have $U_{\tau 1}(\hat{x}) = U_{\tau 1}(0) \equiv U_{\tau 0}$, to be consistent with previous notations. This leaves two unknowns, $\delta_i(\hat{x})$ and $U_{\tau 2}(\hat{x})$, as functions of $\hat{x}$, the fetch on the downstream surface. Therefore, two equations are required to close the system and provide solutions of δ_i and $U_{\tau 2}$.

Elliott approximated the recovering mean velocity profile with a piecewise logarithmic function (illustrated in figure 2*b*),

$$U(z) = \begin{cases} \dfrac{U_{\tau 1}}{\kappa} \ln(z/z_{01}), & z \geqslant \delta_i \\ \dfrac{U_{\tau 2}}{\kappa} \ln(z/z_{02}), & z < \delta_i, \end{cases} \tag{2.3}$$

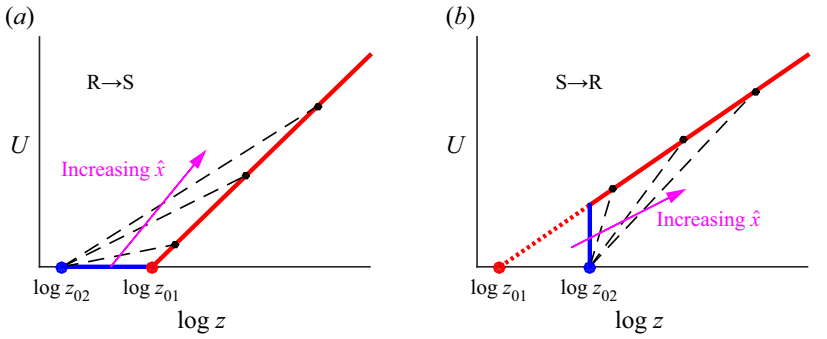

Figure 3. An illustration of the mean velocity profile (2.3) for (*a*) $z_{01} > z_{02}$ (rough-to-smooth) and (*b*) $z_{01} < z_{02}$ (smooth-to-rough). The red lines in both panels are the upstream velocity profile, and the blue line is the velocity profile within the IBL at $\hat{x} = 0$. The black dots are a few representative locations of δ_i farther downstream and the black dashed lines are the velocity profile within the IBL corresponding to these δ_i values.

which implicitly assumes that the mean velocity profile within the IBL immediately adapts to the local wall condition (i.e. that $\delta_i = \delta_e$). From this expression of the mean velocity profile, the first equation to close the system rises naturally as the matching condition, i.e. the two log laws intersecting at $z = \delta_i$:

$$\frac{U_{\tau 1}}{\kappa} \ln(\delta_i/z_{01}) = \frac{U_{\tau 2}}{\kappa} \ln(\delta_i/z_{02}). \tag{2.4}$$

A series of the velocity profiles with various δ_i values are shown in figure 3.

Considering a control volume which has a streamwise width of dx and is bounded by the wall and the IBL height (shown by the dashed line in figure 2*a*), and balancing the streamwise momentum fluxes across the control surface with the net shear stress applied on the top and bottom surfaces, a second equation can be obtained,

$$\frac{\mathrm{d}}{\mathrm{d}x} \int_{z_{02}}^{\delta_i} U^2(\hat{x}, z)\, \mathrm{d}z - U_i(\hat{x}) \frac{\mathrm{d}}{\mathrm{d}x} \int_{z_{02}}^{\delta_i} U(\hat{x}, z)\, \mathrm{d}z = \frac{\Delta\tau(\hat{x})}{\rho}, \tag{2.5}$$

where $\Delta\tau(\hat{x}) = \tau(\hat{x}, \delta_i(\hat{x})) - \tau(\hat{x}, 0)$. The shear stress at the wall is $\tau(\hat{x}, 0) = \rho U_{\tau 2}^2(\hat{x})$ by definition, while Elliott assumed that the upper boundary of the control volume resides within the constant-stress layer which preserves the shear stress of the upstream surface, i.e. $\tau(\hat{x}, \delta_i) = \rho U_{\tau 1}^2$. Therefore, the net shear stress term can be expressed as $\Delta\tau(\hat{x}) = \rho U_{\tau 1}^2 - \rho U_{\tau 2}^2(\hat{x})$. The lower bound of the integral, z_{02}, is chosen as the lowest wall-normal position where the logarithmic U profile is negative according to the mean velocity profile in (2.3). To simplify the notation, we denote the mean velocity at $z = \delta_i$ as U_i, i.e. $U_i(\hat{x}) \equiv U(\hat{x}, \delta_i)$.

With these two equations (2.4) and (2.5), the system will be closed and the evolution of $U_{\tau 2}$ and δ_i can be solved. The growth of δ_i is driven by the source term, $\Delta\tau(\hat{x})/\rho$, which is essentially the difference in the shear stress between the lower and upper control surfaces. The recovering downstream friction velocity $U_{\tau 2}(\hat{x})$ asymptotes to $U_{\tau 1}$. In fact, the streamwise evolution of the flow will only terminate when $U_{\tau 2} = U_{\tau 1}$, which is expected at an infinitely long fetch where $\delta_i \gg \max(z_{01}, z_{02})$. That is to say, when δ_i is infinitely large, in figure 2(*b*) the velocity profile in the IBL (blue line) will eventually be parallel with the upstream velocity profile (red line), thus $U_{\tau 2} = U_{\tau 1}$.

3. Numerical implementation of Elliott's 1958 model

Elliott (1958) solved the ordinary differential equation (ODE) (2.5) analytically. This approach is highly dependent on the analytical form of the mean velocity profile and it can be tedious or even impossible to find an algebraic solution when the functional form of the mean velocity profile changes. Alternatively, we may consider the integral form of (2.5). We first consider a change of variable with δ_i replacing $\hat{x}$ as the independent variable, and apply substitutions

$$G_1(\delta_i) = \int_{z_{02}}^{\delta_i} U(\delta_i, z)\,\mathrm{d}z, \quad G_2(\delta_i) = \int_{z_{02}}^{\delta_i} U^2(\delta_i, z)\,\mathrm{d}z \tag{3.1a,b}$$

to (2.5), resulting in

$$\frac{\mathrm{d}G_2(\delta_i)}{\mathrm{d}x(\delta_i)} - U_i(\delta_i)\frac{\mathrm{d}G_1(\delta_i)}{\mathrm{d}x(\delta_i)} = \frac{\Delta\tau(\delta_i)}{\rho}. \tag{3.2}$$

Multiplying both sides of the equation by $\mathrm{d}x(\delta_i)$ and integrating with respect to G_1 and G_2 on the left-hand side, and x on the right-hand side gives

$$\hat{x}(\delta_i) = \int_{G_2(\delta_i(0))}^{G_2(\delta_i)} \frac{\rho}{\Delta\tau(\delta_i)}\mathrm{d}G_2(\delta_i) - \int_{G_1(\delta_i(0))}^{G_1(\delta_i)} \frac{\rho U_i(\delta_i)}{\Delta\tau(\delta_i)}\mathrm{d}G_1(\delta_i), \tag{3.3}$$

which is equivalent to (2.5) when $\Delta\tau$ is non-zero.

Here in the integral form (3.3), δ_i rather than $\hat{x}$ is considered as the independent variable for computational convenience, provided that $\mathrm{d}\delta_i/\mathrm{d}\hat{x} \neq 0$. Thus, U_i will be a function of δ_i and the two-dimensional mean velocity field $U(\hat{x}, z)$ will be a function of δ_i and z instead. The initial condition of the IBL evolution is $\delta_i(0)$, i.e. $\delta_i(0) = \delta_i$ at $\hat{x} = 0$. The choice of $\delta_i(0)$, provided small, will only lead to a constant displacement in $\hat{x}$ without changing the shape of the predicted δ_i trajectories (see Appendix C). In practice, an array of δ_i locations is first generated, which subsequently determines $U_{\tau 2}(\delta_i)$ and the mean velocity profile $U(\delta_i, z)$ using (2.4), the relation from matching the mean velocity profile at δ_i. The fetch $\hat{x}$ corresponding to each δ_i will then be computed from (3.3) numerically. Compared with the original solution of Elliott (1958), this approach can easily accommodate velocity profiles with more complicated functional forms, which will largely serve our intention in refining the model assumptions. We also note that when presenting the model predictions graphically, we revert to the previous convention of plotting physical quantities against $\hat{x}$ to be consistent with the literature. From here on, this model will be referred to as the E58 model.

3.1. *Evaluating the E58 model*

We first evaluate the E58 model by comparing the experimental data (Li *et al.* 2021) with predictions at matched flow conditions. Two groups of wind tunnel experiments are designed to separately examine the effect of friction Reynolds number and roughness Reynolds number on the flow recovery from a rough-to-smooth change. The friction and roughness Reynolds numbers are defined as $Re_{\tau 0} \equiv U_{\tau 0}\delta_0/\nu$ and $k_{s0}^+ \equiv U_{\tau 0}k_s/\nu$, respectively, and are both evaluated based on conditions over the rough surface just upstream of the roughness transition. The Group-Re consists of measurements with varying $Re_{\tau 0}$ while holding k_{s0}^+ constant, while Group-ks measurements vary k_{s0}^+ while holding $Re_{\tau 0}$ constant. The same P24 grit sandpaper is used in all cases, ensuring a constant k_s, and the variation in $Re_{\tau 0}$ and k_{s0}^+ is achieved by adjusting U_∞, the free stream velocity, and x_0, the streamwise length of the sandpaper patch. The magnitude of the

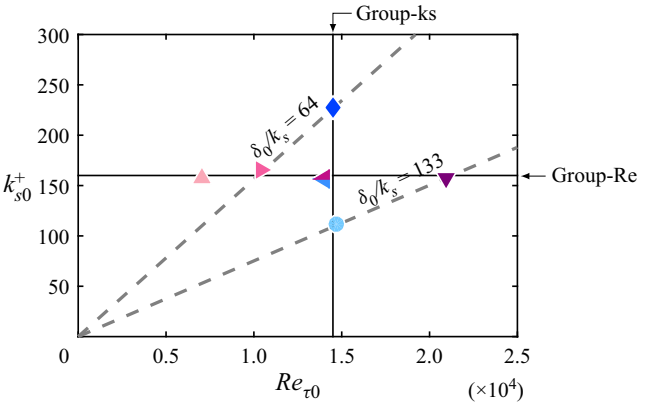

Figure 4. Flow conditions ($Re_{\tau 0}$ and k^+_{s0}) at the immediate upstream of the roughness transition of all cases. All symbols are defined in table 1. The horizontal line is at $k^+_{s0} = 160$, and the vertical line is at $Re_{\tau 0} = 14\,500$. The two dashed lines show the cases with matched δ_0/k_s of 64 and 133. Adapted from Li *et al.* (2021).

	Case	Sym.	$Re_{\tau 0}$	k^+_{s0}	M	x_0 (m)	U_∞ (m s^{-1})	δ_0 (m)	
Group-Re	Re07ks16	▲	7100	158	−3.06	4.5	21.5	0.11	
	Re10ks16	▶	10 400	165	−3.08	7.2	22.5	0.15	
	Re21ks16	▼	21 000	157	−3.05	17.1	24.3	0.32	
	Re14ks16	◀	14 000	157	−3.08	11.1	23.3	0.22	Group-ks
	Re14ks11	●	14 700	111	−2.73	17.1	17.0	0.32	
	Re14ks22	◆	14 500	228	−3.41	7.2	31.0	0.15	

Table 1. Summary of the experimental cases. The friction velocity $U_{\tau 0}$ employed in calculating $Re_{\tau 0}$ and k^+_{s0} is obtained over the rough fetch just upstream of the rough-to-smooth transition. Note that case Re14ks16 is shared between Group-Re and Group-ks, therefore its symbol can take either pink or blue colour in the corresponding group. Adapted from Li *et al.* (2021).

surface roughness change is denoted by $M \equiv \ln(z_{02}/z_{01})$, where z_{02} is calculated from the maximum $U_{\tau 2}$ measured downstream of the transition. Legends and flow conditions of the cases are summarised in table 1 and the $Re_{\tau 0}$–k^+_{s0} parameter space is shown in figure 4. For further experimental details of these cases, readers are referred to the paper by Li *et al.* (2021).

In the original formulation of Elliott's model, the incoming flow is a deep surface layer where neither δ_0 nor U_∞ (therefore C_f) is defined. It is also applicable to a flat plate boundary layer with a finite thickness where δ_i is only a small fraction of the entire boundary layer. Based on the dimensional argument, the flow should be independent of δ_0 in the limit of small δ_i/δ_0. For a smooth downstream surface, the piecewise mean velocity profile (2.3) can be rewritten as

$$U(z) = \begin{cases} \dfrac{U_{\tau 1}}{\kappa} \ln(z/z_{01}), & z \geqslant \delta_i \\ U_{\tau 2}\left(\dfrac{1}{\kappa}\ln(zU_{\tau 2}/\nu) + B\right), & z < \delta_i, \end{cases} \tag{3.4}$$

and the kinematic viscosity of the fluid ν instead of a roughness length z_{02} is introduced to the problem. When choosing $U_{\tau 0}$ as the velocity scale and $\nu/U_{\tau 0}$ as the length scale, the incoming flow condition can be fully described by a non-dimensional number k_{s0}^{+}, provided that δ_0 is large so it does not enter the problem. This implies that for the E58 model, both $U_{\tau 2}/U_{\tau 0}$ and $\delta_i U_{\tau 0}/\nu$ in Group-Re, where k_{s0}^{+} is held constant, should collapse to a single trend despite the changes in $Re_{\tau 0}$. The comparison of these theoretical results with experimental data is discussed below.

3.2. *Friction velocity* $U_{\tau 2}$

The measured and predicted recovering friction velocity $U_{\tau 2}$ on the downstream surface is plotted against fetch $\hat{x}$ in figure 5, using $U_{\tau 0}$ and $\nu/U_{\tau 0}$ as the velocity and length scales, respectively. The Group-Re results are shown in figure 5(*a*), where a single curve represents the prediction of the E58 model for all four cases, since $Re_{\tau 0}$ (essentially the outer length scale) was not a parameter in the original model. Over a limited range of $\hat{x}U_{\tau 0}/\nu < 1 \times 10^5$, the measurements follow the prediction closely with no distinguishable trend with $Re_{\tau 0}$. The Group-ks data are presented in figure 5(*b*), where a greater drop in the friction velocity downstream is observed with a higher k_{s0}^{+}. The good agreement between the data points and the model prediction indicates that such a dependence on k_{s0}^{+} is generally well captured by the E58 model.

However, the zoomed views as shown in figures 5(*c*) and 5(*d*) reveal the under-estimation of the E58 model in the near field ($0 < \hat{x}U_{\tau 0}/\nu < 0.05 \times 10^5$). Since the mean velocity within and above the IBL are modelled by two logarithmic laws, the flow recovery in the near vicinity of the step change will not be captured correctly by the E58 model due to the deviation from a canonical smooth-wall mean velocity profile as detailed in Li *et al.* (2019, 2021). In addition, the adequacy of the model is also expected to drop when δ_i exceeds the upper limit of the logarithmic layer (chosen as $z/\delta_{99} = 0.15$ in this study), as the E58 model fails to capture the wake region. In figure 5, the data points with $\delta_i/\delta_{99} < 0.15$ are shown by solid symbols, while the rest are shown by open symbols. For all solid symbols, the model prediction follows the measured results closely (excluding the near field). This good agreement still exists even after δ_i exceeds $0.15\delta_{99}$, until it reaches approximately $0.6\delta_{99}$ (shown by the symbols with a thick black outline). The model appears valid for a wider range of δ_i/δ_{99} than would be expected. One possible explanation is that the effects from those factors which are not accounted for in the E58 model, such as the inclusion of a wake function or the growth of the outer layer downstream, tend to cancel out. This will be discussed in more detail in § 4. It is also noticed in figure 5(*a*) that cases with a higher $Re_{\tau 0}$ in Group-Re follow the model prediction for a longer $\hat{x}U_{\tau 0}/\nu$, as a longer $\hat{x}U_{\tau 0}/\nu$ is required before δ_i/δ_{99} reaches 0.6. After δ_i exceeds $0.6\delta_{99}$, the experimentally determined $U_{\tau 2}/U_{\tau 0}$ starts to decrease with $\hat{x}U_{\tau 0}/\nu$ in both groups, in contrast to the model predictions. For cases in Group-Re, $U_{\tau 2}/U_{\tau 0}$ is observed to fan out and increase with $Re_{\tau 0}$ at $\hat{x}U_{\tau 0}/\nu \gtrsim 1 \times 10^5$, which can be broadly explained as follows. Neglecting the growth in δ_{99}, the asymptotic value of fully recovered $U_{\tau 2}/U_{\tau 0}$ can be written as

$$U_{\tau 2}/U_{\tau 0} = \frac{\sqrt{2/C_f} - \Delta U^{+}}{\sqrt{2/C_f}}. \tag{3.5}$$

Since k_{s0}^{+} is constant in Group-Re, ΔU^{+} will also be a constant, while $\sqrt{2/C_f}$ increases with an increasing $Re_{\tau 0}$. Therefore, the ratio $U_{\tau 2}/U_{\tau 0}$ also increases with $Re_{\tau 0}$. A rigorous theoretical proof of this is detailed in Appendix A.

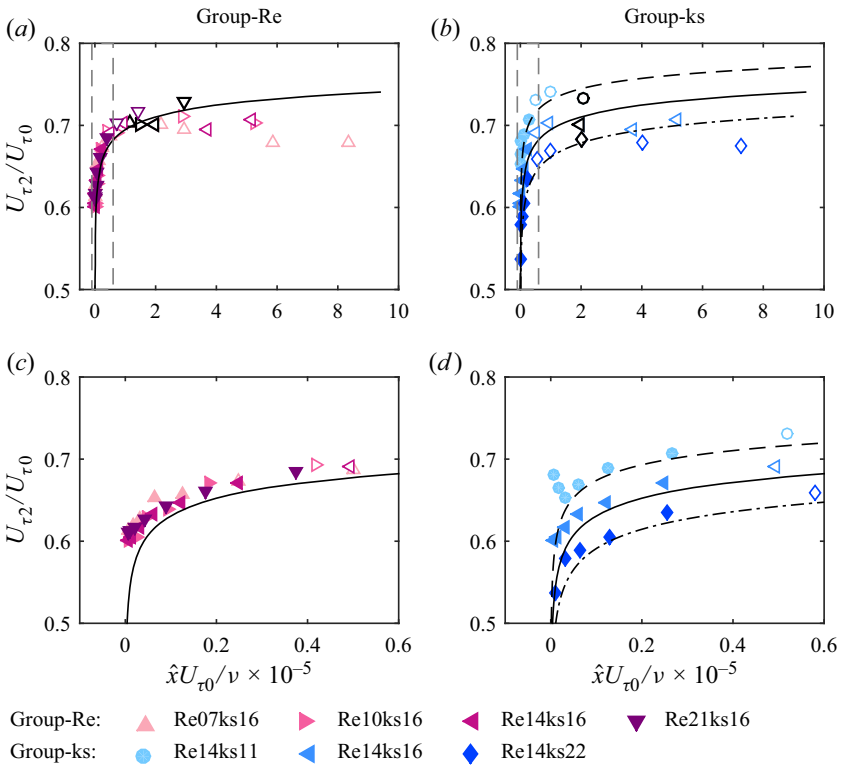

Figure 5. Friction velocities on the smooth surface normalised by $U_{\tau 0}$, the friction velocity on the rough surface versus the viscous-scaled fetch $\hat{x}U_{\tau 0}/\nu$ for (*a*) Group-Re and (*b*) Group-ks. Panels (*c*) and (*d*) are the corresponding magnified view in the near field. The solid lines in all figures are predictions using the E58 model with $k_{s0}^{+} = 160$, while the dashed and dash-dotted lines in (*b*) and (*d*) are with $k_{s0}^{+} = 110$ and $k_{s0}^{+} = 230$, respectively. Data points with $\delta_i/\delta_{99} < 0.15$ are shown by solid symbols, while the rest are shown by open symbols. Symbols with a thick black outline are at $\delta_i/\delta_{99} \approx 0.6$.

3.3. *The IBL height δ_i*

As mentioned in § 2, $U_{\tau 2}$ and δ_i are coupled through the assumed mean velocity profile in Elliott's model. The mean velocity profile is modelled by a piecewise logarithmic function, with a slope proportional to $U_{\tau 2}$ below δ_i, and $U_{\tau 0}$ above δ_i. Here we examine the validity of this assumption by reconstructing the inner logarithmic profile as $U_{log}^{+} = (1/\kappa)\ln(z^{+}) + B$, where $^{+}$ denotes an inner normalisation with the local $U_{\tau 2}$. The comparison between the experimentally measured U^{+} and predicted inner log region U_{log}^{+} is shown in figure 6. Elliott's IBL height δ_i is defined as the wall-normal location where $U^{+} - U_{log}^{+} = 0$, or where the smooth-wall logarithmic profiles intersect the measured mean velocity profile, as represented by the black crosses, and we will denote it by $\delta_{i,log}$. This definition is essentially dependent on the local $U_{\tau 2}$ value rather than the shape of the measured mean velocity profiles below δ_i. If the mean velocity profile is the same as assumed by Elliott, then $\delta_{i,log}$ should coincide with the profile-based δ_i results. Figure 6 shows two additional profiles based estimates of δ_i. The circles show δ_i determined from the variance profiles following the approach in Li *et al.* (2021), while the solid pink symbol with the black outline shows δ_i estimated from U versus $z^{1/2}$ profile following Antonia & Luxton (1971). Both profile-based estimates are in good agreement with each other (despite a small systematic difference), while both are much lower than $\delta_{i,log}$ which is

shown by the open pink symbol. A comparison of the δ_i values within the logarithmic region is shown in figure 7. Note that the method to compute Elliott's $\delta_{i,log}$ is only expected to perform well within the logarithmic region: when $\delta_{i,log}$ enters the wake region, the intersecting location will remain as the upper limit of the logarithmic region regardless of the shape of the profile. Therefore, only $\delta_{i,log} < 0.15\delta_{99}$ are shown in figure 7. In both Group-Re and Group-ks, $\delta_{i,log}$ is systematically higher than the δ_i calculated following our current approach. This observation reiterates our previous conclusion that the mean flow within the IBL has not yet fully recovered to a canonical smooth-wall profile, and it also provides some useful clues in refining Elliott's original model. In fact, $\delta_{i,log}$ can be approximated by the following empirical equation at least in the near field:

$$\frac{\delta_{i,log}U_{\tau 0}}{\nu} \approx \frac{\delta_i U_{\tau 0}}{\nu} + \Delta\delta_i^+. \tag{3.6}$$

The additive constant $\Delta\delta_i^+ \approx 500$ is obtained based on empirical observation, and it appears to apply within the range of $Re_{\tau 0}$ and k_{s0}^+ available in this study, which may be interpreted as a constant level of deviation from the canonical smooth-wall state. It is not clear whether this additive constant will change in the case of extreme $Re_{\tau 0}$ or k_{s0}^+ values. Future work is required to fully address this question. The predicted IBL thickness is also included in figure 7. The E58 model predicts that the viscous-scaled IBL thickness $\delta_i U_{\tau 0}/\nu$ will grow slightly faster with a higher upstream k_{s0}^+, as shown in figure 7(*b*). The comparison with the E58 model suggests that for the range of k_{s0}^+ investigated here, we would struggle (within experimental error) to see any difference in the development of δ_i in the Group-ks experimental data. If k_{s0}^+ effects on the growth rate of δ_i are to be investigated, a much larger variation of k_{s0}^+, or perturbation strength M will be required. As shown in figure 7, the E58 model under-predicts $\delta_{i,log}$, suggesting the necessity in improving the assumptions in the E58 model. However, it is noted that the model predictions are closer to the δ_i values determined from variance profiles, although these two quantities have different physical meaning.

4. Finite-thickness boundary layer: a refined model

Elliott (1958) originally considered a thick surface layer where the total boundary layer thickness is irrelevant in the problem and the mean velocity profile can be modelled by a logarithmic law over the entire range of z to predict the quantities of interest. In most engineering applications, however, the boundary layers have a finite thickness and the growth of the IBL may be affected when it exceeds the logarithmic layer and enters the wake region (figure 8). In this section, we adapt the E58 model to accommodate such scenarios with a focus on the outer layer behaviour.

In particular, we continue within the framework of Elliott, which is to satisfy the streamwise momentum equation by adjusting the local length and velocity scales in an assumed velocity profile. However, the form of the assumed velocity profile and momentum equation(s) need to be modified for a finite-thickness boundary layer (FTBL). First, the mean velocity profile deviates from the logarithmic law in the outer layer, which can be modelled by a wake function (§ 4.1). Second, alongside the growth of the IBL, the thickness of whole boundary layer also increases spatially, modifying $U_{\tau 1}$, the local friction velocity scale of the outer layer (§ 4.2). Finally, the constant-stress layer assumption is not applicable beyond the logarithmic layer, and in § 4.3 we replace it with a more realistic wall-normal shear-stress distribution which decreases to 0 at the edge of the boundary layer. This model will be denoted as FTBL. Further, the deviation of the

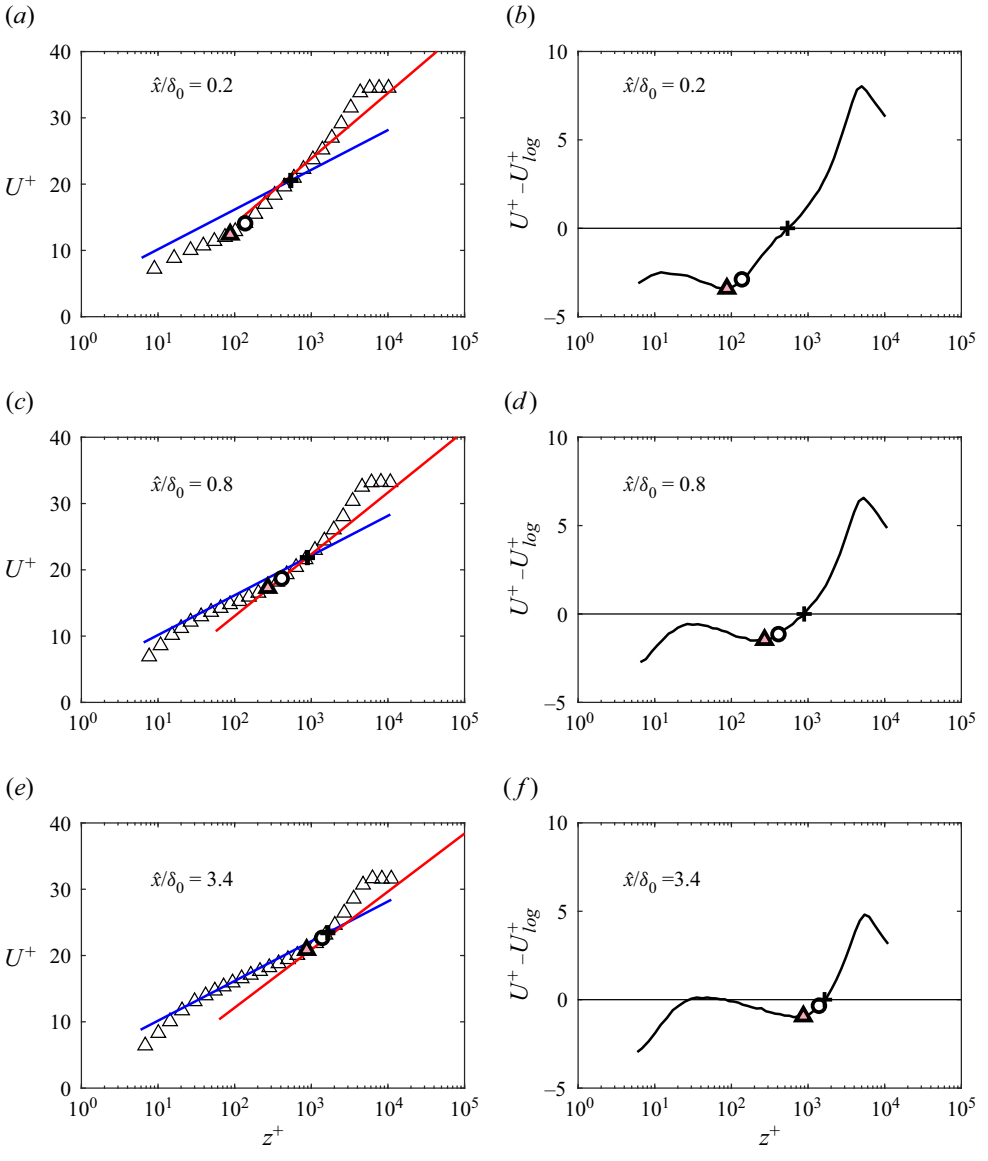

Figure 6. (*a*,*c*,*e*) Comparison between U^+ (empty triangles), the viscous-scaled mean velocity profile downstream of the step change, inner logarithmic profile $U^+_{log} = (1/\kappa)\ln(z^+) + B$ (solid blue line) and outer logarithmic profile (solid red line) for case Re07ks16. Panels (*b*,*d*,*f*) show the difference between U^+ and U^+_{log} at streamwise locations corresponding to (*a*,*c*,*e*), respectively. Black '+' symbols represent the wall-normal position where $U^+ - U^+_{log} = 0$, circles represent δ_i computed using the variance-profile-based approach detailed in Li *et al.* (2021), and the triangles with a thick black outline represent δ_i defined as the inflection point in the U versus $z^{1/2}$ profile (Antonia & Luxton 1971).

mean velocity profile from the log-law in a recovering internal layer can be modelled by the blending function, as introduced by Li *et al.* (2021), and this variation of the model (introduced in § 4.4) will be denoted as FTBL-B.

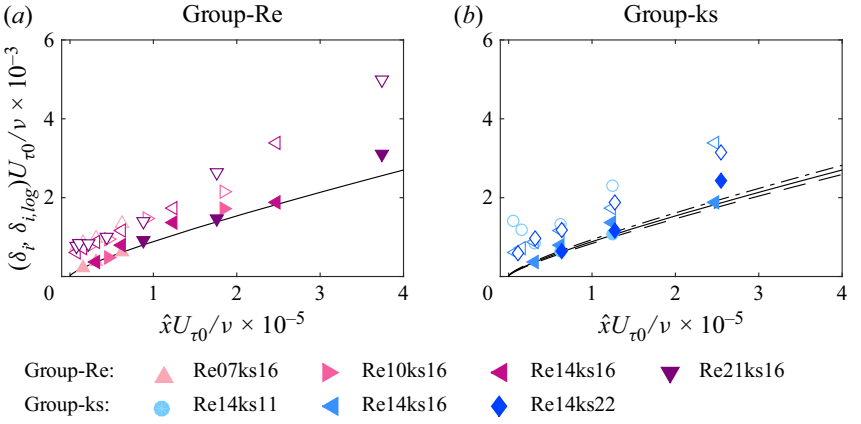

Figure 7. Comparison of δ_i determined using the current variance-profile-based approach (solid symbols) and $\delta_{i,log}$, the wall-normal position where $U^+ - U^+_{log} = 0$ (empty symbols) for (*a*) Group-Re and (*b*) Group-ks cases. The solid lines in both columns are predictions using the E58 model with $k^+_{s0} = 160$, while the dashed and dash-dotted lines in (*b*) are with $k^+_{s0} = 110$ and $k^+_{s0} = 230$, respectively.

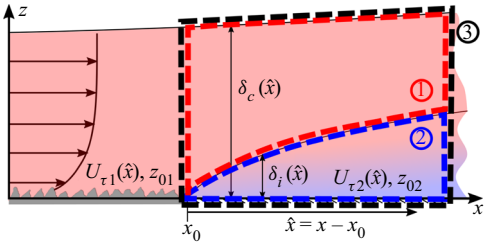

Figure 8. Schematic of the IBL with a finite outer layer height $\delta_c(\hat{x})$ that grows in the streamwise direction. The flow direction is from left to right. A step change from rough to smooth is currently depicted in the figure, but the FTBL model is also applicable to other scenarios (e.g. smooth-to-rough or rough-to-rougher). The control volumes are delineated by thick dashed borderlines.

4.1. *Wake function*

We first introduce an additional variable, δ_c, as a representation of the boundary layer thickness, and adopt the expression of the wake function given by Jones, Marusic & Perry (2001),

$$\mathcal{W}(\eta) = -\frac{1}{3\kappa}\eta^3 + \frac{\Pi}{\kappa}[2\eta^2(3-2\eta)], \tag{4.1}$$

where $\eta \equiv z/\delta_c$. The mean velocity profile has zero gradient at $z = \delta_c$, and typically $\delta_c \approx 1.2\delta_{99}$ for a smooth-wall turbulent boundary layer at a moderate Reynolds number. Here, $\Pi = 0.56$ (corresponding to a Coles wake strength of $\Pi_c = 0.42$, as reported by Marusic *et al.* (2015) from data obtained in the Melbourne High Reynolds Number Wind Tunnel). To summarise, the mean velocity profile is modified as

$$U(z) = \begin{cases} \dfrac{U_{\tau 1}}{\kappa}\ln\left(\dfrac{z}{z_{01}}\right) + U_{\tau 1}\mathcal{W}\left(\dfrac{z}{\delta_c}\right), & \text{for } z \geqslant \delta_i, \\ \dfrac{U_{\tau 2}}{\kappa}\ln\left(\dfrac{z}{z_{02}}\right) + U_{\tau 2}\mathcal{W}\left(\dfrac{z}{\delta_c}\right), & \text{for } z < \delta_i. \end{cases} \tag{4.2}$$

Here we assume that the internal and outer boundary layers (below and above δ_i) perceive the same overall boundary layer thickness δ_c, and the mixing of both logarithmic profiles in (4.2) with the free stream flow occur at the same distance from the wall (approximately $0.15\delta_c$). This can be justified, at least in the limits: close to the roughness change where $\delta_i \to 0$, the contribution from the wake function to the internal velocity profile is negligible, and the outer layer remains unchanged from the incoming boundary layer. Very far downstream of the roughness change where $\delta_i \to \delta_c$, the boundary layer has almost fully adapted to the new surface condition, and the expression (4.2) reduces to a profile in equilibrium with the local wall conditions.

The velocity matching condition at $z = \delta_i$ consequently becomes

$$U(\delta_i) = \frac{U_{\tau 1}}{\kappa} \ln\left(\frac{\delta_i}{z_{01}}\right) + U_{\tau 1}\mathcal{W}\left(\frac{\delta_i}{\delta_c}\right) = \frac{U_{\tau 2}}{\kappa} \ln\left(\frac{\delta_i}{z_{02}}\right) + U_{\tau 2}\mathcal{W}\left(\frac{\delta_i}{\delta_c}\right). \tag{4.3}$$

4.2. *Streamwise evolution of the outer layer*

In contrast to the E58 model, we introduce δ_c, the thickness of the entire boundary layer (§ 4.1), which grows with $\hat{x}$, and $U_{\tau 1}$ is no longer treated as a constant. Therefore, two more unknowns $\delta_c(\hat{x})$ and $U_{\tau 1}(\hat{x})$ are added to the problem, and two more equations are required to close the system. A refined schematic of the problem is shown in figure 8.

We assume that the evolution of the outer layer is not directly affected by the presence of the IBL. The outer-layer friction velocity $U_{\tau 1}(\hat{x})$ can be determined by ensuring that the mean velocity profile satisfies the boundary condition of $U = U_\infty$ at $z = \delta_c$:

$$\frac{U_\infty}{U_{\tau 1}} = \frac{1}{\kappa} \ln\left(\frac{\delta_c}{k_s}\right) + A'_{FR} + \frac{2\Pi}{\kappa}\mathcal{W}(1). \tag{4.4}$$

Note that now both $U_{\tau 1}$ and δ_c are functions of $\hat{x}$ and their values will change in the streamwise direction as the outer layer evolves. We can also introduce the von Kármán momentum integral equation of the entire boundary layer (control volume ① in figure 8),

$$\frac{\mathrm{d}\theta}{\mathrm{d}\hat{x}} = \frac{U_{\tau 2}^2}{U_\infty^2}, \tag{4.5}$$

where $\theta = \int_{z_{02}}^{\delta_c} (U_\infty - U)U/U_\infty^2 \,\mathrm{d}z$ is the momentum thickness of the entire boundary layer. The momentum integral equation can be rearranged and further integrated with respect to θ as

$$\hat{x} = \int_{\theta(\delta_i(0))}^{\theta(\delta_i)} \frac{U_\infty^2}{U_{\tau 2}^2} \mathrm{d}\theta. \tag{4.6}$$

These two equations (4.4) and (4.6), together with (2.4) and (3.3) which govern the flow within the IBL, can fully determine the four unknowns ($U_{\tau 2}$, δ_i, $U_{\tau 1}$ and δ_c) of the system.

4.3. *Shear-stress correction*

In a turbulent boundary layer, the total shear stress τ is contributed by the wall-normal gradient in the mean flow and the Reynolds shear stress:

$$\tau^+ = \frac{\mathrm{d}U^+}{\mathrm{d}z^+} - \overline{uw}^+. \tag{4.7}$$

The first term only dominates in the viscous sublayer, and the contribution is mainly from the Reynolds shear stress (the second term) above the buffer region. In the limit

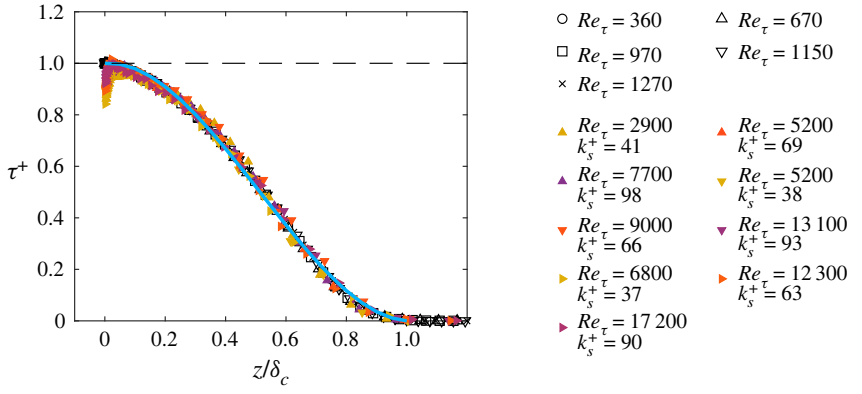

Figure 9. Shear stress normalised by the friction velocity at the wall and plotted against the wall position normalised by Jones' boundary layer thickness. The coloured symbols are multiwire hot-wire data obtained from turbulent boundary layers developed on a sandpaper roughness (Morrill-Winter *et al.* 2017). The black empty symbols are direct numerical simulation (DNS) data of a smooth-wall boundary layer (Schlatter & Örlü 2010). The thick blue line is (4.8) and the horizontal dashed line is at $\tau^+ = 1$.

of asymptotically high Reynolds numbers, a constant-stress layer forms in the logarithmic region with τ^+ remaining at unity as determined by the equations of motion (Tennekes & Lumley 1972, p. 54). This assumption is adequate in the E58 model, posed for the atmospheric surface layer, because δ_i remains in the logarithmic layer throughout the evolution and Reynolds numbers are typically very high. However, the validity of this assumption diminishes when a finite-thickness turbulent boundary layer is considered. In the wake region, the Reynolds shear stress is observed to decrease significantly to $0.5\tau_w$ at $z \approx 0.5\delta_c$ (Antonia & Luxton 1972; Schlatter & Örlü 2010; Morrill-Winter *et al.* 2017). Shear stress data from both experiments and DNS of spatially developing canonical boundary layers are summarised in figure 9. Both rough-wall and smooth-wall boundary layer data with a wide range of Re_τ and k_s^+ are included. Here τ^+ decreases steadily from 1 in the near-wall region to 0 in the free stream. The approximation of a constant stress, i.e. $\tau^+ = 1$, is reasonable for $z/\delta_c < 0.15$, while the deviation from this approximation is significant above the logarithmic region. A good collapse of the data at various Reynolds numbers is observed under the current scaling. We then fit a third-order polynomial

$$\tau^+ = p_1\left(\frac{z}{\delta_c}\right)^3 + p_2\left(\frac{z}{\delta_c}\right)^2 - (1 + p_1 + p_2)\frac{z}{\delta_c} + 1 \tag{4.8}$$

(which is constrained to $\tau^+ = 1$ at $z = 0$ and $\tau^+ = 0$ at $z/\delta_c = 1$) to the data in the range of $0.1 < z/\delta_c < 1$, and the fitting parameters are found to be $p_1 = 1.9971$ and $p_2 = -3.0789$.

Here we propose a modification of the term $\Delta\tau_2$, which is the difference between the shear stress at the top and bottom surfaces of control volume ② in figure 8, by replacing the stress at $z = \delta_i$ with the aforementioned empirical fit (4.8) that captures the decrease of the shear stress in the wake region. The shear-stress difference $\Delta\tau_2$ becomes

$$\Delta\tau_2 = \rho U_{\tau 1}^2\left[p_1\left(\frac{\delta_i}{\delta_c}\right)^3 + p_2\left(\frac{\delta_i}{\delta_c}\right)^2 - (1 + p_1 + p_2)\frac{\delta_i}{\delta_c} + 1\right] - \rho U_{\tau 2}^2. \tag{4.9}$$

In the rough-to-smooth case, as δ_i/δ_c increases from 0 to 1, the sign of $\Delta\tau_2$ changes from positive to negative with a zero-crossing point in between, which will cause a

division-by-zero issue in (3.3). To circumvent this problem, we consider a control volume bounded by $z = \delta_i$ and $z = \infty$ (① in figure 8), rather than the one between $z = 0$ and $z = \delta_i$ employed by Elliott to derive (2.5). In place of (3.3), the following momentum equation of control volume ①, which is obtained by subtracting (4.6) from (2.5), is used in the evolution:

$$-\frac{\mathrm{d}}{\mathrm{d}x}\int_{\delta_i}^{\infty} U^2(\hat{x}, z)\,\mathrm{d}z + \left(U_\infty - U_i(\hat{x})\right)\frac{\mathrm{d}}{\mathrm{d}x}\int_{z_{02}}^{\delta_i} U(\hat{x}, z)\,\mathrm{d}z + U_\infty\frac{\mathrm{d}}{\mathrm{d}x}\int_{\delta_i}^{\infty} U(\hat{x}, z)\,\mathrm{d}z = \frac{\Delta\tau_1(\hat{x})}{\rho}. \tag{4.10}$$

Here,

$$\Delta\tau_1 = \rho U_{\tau 1}^2\left[p_1\left(\frac{\delta_i}{\delta_c}\right)^3 + p_2\left(\frac{\delta_i}{\delta_c}\right)^2 - (1 + p_1 + p_2)\frac{\delta_i}{\delta_c} + 1\right], \tag{4.11}$$

which will remain positive until $\delta_i = \delta_c$.

After eliminating $\hat{x}$ from the integral form of (2.5) and (4.6), the equations reduce to

$$-\int_{G_4(\delta_i(0))}^{G_4(\delta_i)}\frac{1}{\Delta\tau_1}\mathrm{d}G_4 + \int_{G_1(\delta_i(0))}^{G_1(\delta_i)}\frac{U_\infty - U_i}{\Delta\tau_1}\mathrm{d}G_1 + U_\infty\int_{G_3(\delta_i(0))}^{G_3(\delta_i)}\frac{1}{\Delta\tau_1}\mathrm{d}G_3 - \frac{U_\infty^2}{\rho}\int_{\theta(\delta_i(0))}^{\theta(\delta_i)}\frac{1}{U_{\tau 2}^2}\mathrm{d}\theta = 0 \tag{4.12}$$

and

$$G_3(\delta_i) = \int_{\delta_i}^{\infty} U(\delta_i, z)\,\mathrm{d}z, \qquad G_4(\delta_i) = \int_{\delta_i}^{\infty} U^2(\delta_i, z)\,\mathrm{d}z. \tag{4.13a,b}$$

This together with (4.3) and (4.4) form a system of three equations, which are the governing equations of the FTBL model. For a given δ_i, the corresponding δ_c, $U_{\tau 1}$ and $U_{\tau 2}$ can be solved numerically using the Newton–Raphson method (Atkinson 1989, p. 58). The Newton–Raphson approach is coded in MATLAB. The only two input parameters required from the user are $Re_{\tau c0}$ and k_{s0}^+ for non-dimensional predictions. Additionally, the free stream velocity U_∞ and equivalent sand grain roughness k_s are needed to retrieve dimensional predictions. The MATLAB program is validated by comparing its results with those obtained from an alternative method. With a simpler piecewise logarithmic velocity profile, the system of ODEs (4.3), (4.4) and (4.10) can be analytically expressed and solved numerically in Mathematica. Both programs are available as supplementary materials available at https://doi.org/10.1017/jfm.2022.731. These two methods produce the same predictions, as shown in figure 10.

Here onwards, we will continue to use the Newton–Raphson approach because it allows choices of more sophisticated velocity profiles such as the blending profile. In figure 11, the predictions from the FTBL model of both rough-to-smooth and smooth-to-rough cases are compared with those of the E58 model. As shown in figure 11(*a*), for both surface arrangements, the FTBL model results in a slower growth of δ_i, potentially as a consequence of the shear-stress correction. At matched friction and roughness Reynolds numbers, the IBL growth is more rapid following a smooth-to-rough change than a rough-to-smooth one. This agrees qualitatively with the experimental observation of Antonia & Luxton (1971, 1972), who attributed the slow growth of δ_i in the rough-to-smooth case to the fact that it is a relaxation process. Figure 11(*b*) shows the

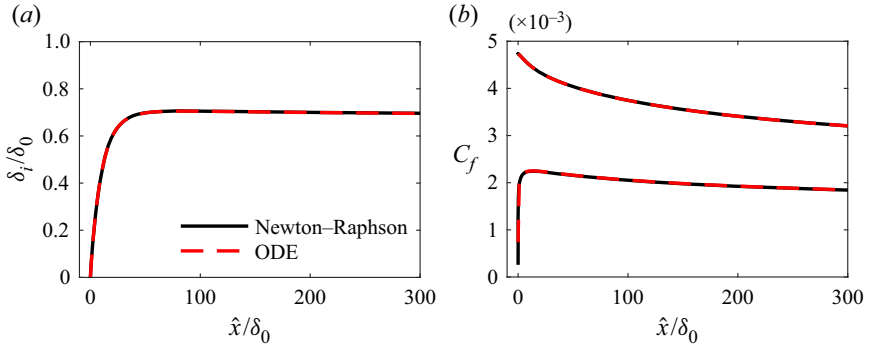

Figure 10. Results obtained by solving the integral equations using Newton–Raphson method and by solving the system of ODEs directly in Mathematica. The parameters of the rough-to-smooth change are matched to case Re14ks16 with $k_{s1}U_{\tau 0}/\nu = 160$ and $Re_{\tau c0} = 16\,500$.

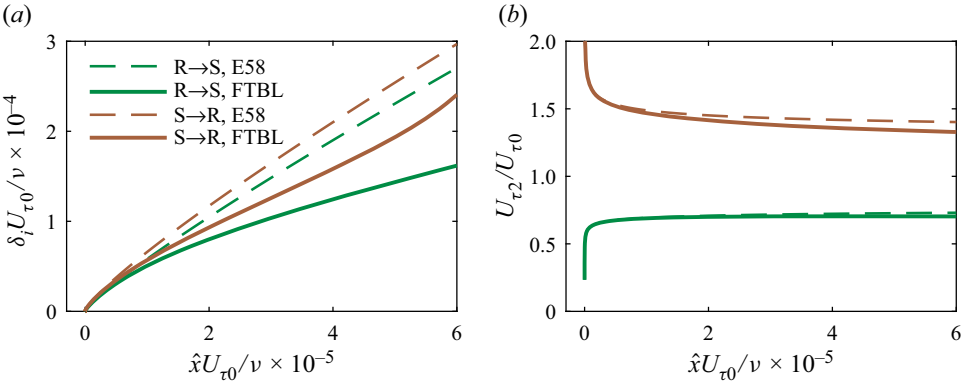

Figure 11. Comparison of the predicted (*a*) IBL height δ_i and (*b*) friction velocity $U_{\tau 2}$ from the E58 and FTBL models. For both rough-to-smooth and smooth-to-rough cases, $\max(k_{s1}, k_{s2})U_{\tau 0}/\nu = 160$ and $Re_{\tau c0} = 16\,500$. The flow conditions of the rough-to-smooth case are matched to case Re14ks16.

predicted $U_{\tau 2}$ for both models and surface arrangements. The overshoot in $U_{\tau 2}$ following a smooth-to-rough change and the undershoot in $U_{\tau 2}$ following a rough-to-smooth one as well as the subsequent recovery are captured by both models. The FTBL model predicts a slightly lower $U_{\tau 2}$ compared with the E58 model for both surface configurations.

The predicted skin-friction coefficient $C_f \equiv 2U_{\tau 2}^2/U_\infty^2$ is shown in figure 12(*b*). Following Baars *et al.* (2016) and Sridhar (2018), the expected C_f of a turbulent boundary layer on a homogeneous wall with the same roughness as the downstream surface can be estimated as

$$C_{fe} = 2\left(\ln\left(Re_\theta\right)/0.38 + 3.7 - \Delta U^+\right)^{-2}, \tag{4.14}$$

where ΔU^+ is the Hama function of the downstream roughness. C_{fe} is shown by the grey lines in figure 12(*a*). Here C_f undershoots C_{fe} in the rough-to-smooth case and overshoots C_{fe} in the smooth-to-rough one, before the difference between the two becomes insignificant at $\hat{x}/\delta_0 \approx 20$. Downstream of this location, C_f decreases with increasing $\hat{x}$ in both cases. The calculation terminates when δ_i reaches δ_c, however, for the rough-to-smooth case, the growth of δ_i in the far field is sensitive to the fit in (4.8). By using a slightly different pair of coefficients ($p_1 = 2.06$ and $p_2 = -3.12$), as shown by

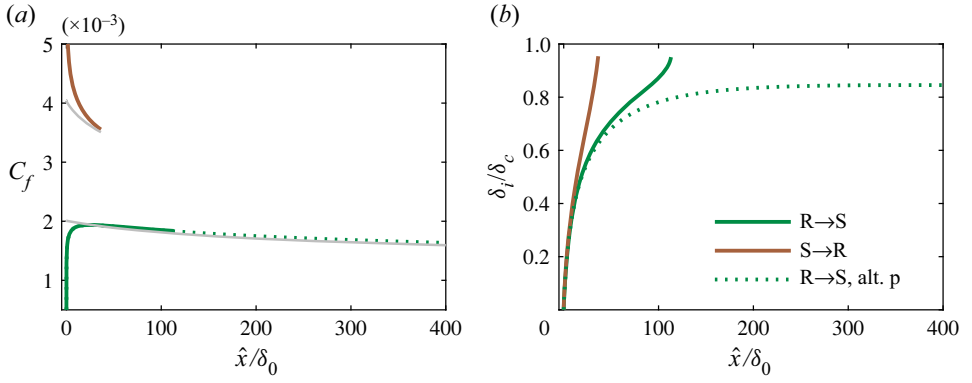

Figure 12. Predictions of the FTBL model with prescribed flow conditions of $\max(k_{s1}, k_{s2})U_{\tau 0}/\nu = 160$ and $Re_{\tau c0} = 16\,500$. The dotted green line represents the rough-to-smooth case with slightly modified coefficients of $p_1 = 2.06$ and $p_2 = -3.12$ in the shear-stress profile (4.8). (*a*) Skin-friction coefficient C_f of the downstream surface plotted against $\hat{x}/\delta_0$. The light grey lines are the corresponding asymptotic values of the downstream surface, estimated using (4.14). (*b*) The IBL thickness δ_i normalised by the local boundary layer thickness δ_c, plotted against streamwise fetch $\hat{x}$ normalised by the boundary layer thickness at the roughness transition.

the dotted line in figure 12(*b*), the ratio δ_i/δ_c plateaus around 0.8 at large $\hat{x}/\delta_0$ instead of reaching 1. However, such differences are relatively inconsequential. At $k_{s0}^+ \sim O(10^2)$ and $Re_{\tau c0} \sim O(10^4)$ as in the present study, when $\delta_i/\delta_c \gtrsim 0.8$, the flow has largely recovered to the undisturbed state of the downstream surface, so the exact location of the IBL is not important. The distinction between the IBL and the outer layer in the mean velocity profile is very small, and it is nearly impossible to distinguish from the measurement noise in an experimental dataset. For the smooth-to-rough case, on the other hand, a small perturbation in the coefficients does not make any significant changes in the predicted δ_i trajectory.

The contribution from each refinement introduced so far in §§ 4.1–4.3 is detailed in Appendix D. Different choices of the wake function and shear-stress profile have also been considered, and they are found to only modify the prediction slightly without changing the $Re_{\tau 0}$ or k_{s0}^+ trends.

4.4. *Recovering flow in the IBL*

So far, the mean velocity profile within the IBL has been modelled by a logarithmic law with a slope determined by the local friction velocity $U_{\tau 2}(\hat{x})$. The non-equilibrium effect of the flow within the IBL, i.e. the deviation from the logarithmic profile (Antonia & Luxton 1972; Li *et al.* 2019; Rouhi *et al.* 2019), is not considered. In this section, we would like to make further improvements by incorporating the blending velocity profile formulated by Li *et al.* (2021), which provides a better representation of the adjusting mean velocity profile for rough-to-smooth transitions.

We first improve the mean velocity representation in the near-wall region with a Musker profile. The full velocity profile can be expressed as

$$U(z) = \begin{cases} \dfrac{U_{\tau 1}}{\kappa} \ln\left(\dfrac{z}{z_{01}}\right) + U_{\tau 1}\mathcal{W}\left(\dfrac{z}{\delta_c}\right), & \text{for } z \geqslant \delta_i, \\ U_{\tau 2} U^+_{Musker}\left(\dfrac{zU_{\tau 2}}{\nu}\right) + U_{\tau 2}\mathcal{W}\left(\dfrac{z}{\delta_c}\right), & \text{for } z < \delta_i, \end{cases} \tag{4.15}$$

where U^+_{Musker} stands for the Musker profile (composite velocity profile excluding the wake function) as used by Chauhan *et al.* (2009) (the expression of the Musker profile is detailed in Appendix B). By assuming that both profiles must simultaneously match at $z = \delta_i$, we also get

$$U(\delta_i) = \frac{U_{\tau 1}}{\kappa} \ln\left(\frac{\delta_i}{z_{01}}\right) + U_{\tau 1}\mathcal{W}\left(\frac{\delta_i}{\delta_c}\right) = U_{\tau 2} U^+_{Musker}\left(\frac{\delta_i U_{\tau 2}}{\nu}\right) + U_{\tau 2}\mathcal{W}\left(\frac{\delta_i}{\delta_c}\right). \quad (4.16)$$

If we consider the lower bound of the logarithmic region as 100 wall units, then for a flow with $Re_\tau \sim O(10^5)$, the viscous sublayer and buffer layer together will only take up 0.1 % of the entire boundary layer thickness. Despite the negligible effect on the predicted results, the inclusion of the Musker profile is useful to facilitate the direct comparison of the mean velocity profiles between the model prediction and experiments. Using the Musker profile also permits further modifications to the velocity profile within the IBL to model the non-equilibrium effect to be detailed below.

We account for the non-equilibrium behaviour of the mean flow within the IBL by replacing the mean velocity profile (4.2) with a blending model as formulated empirically by Li *et al.* (2021). The recovering mean velocity profile is constructed from blending canonical smooth-wall and rough-wall boundary layer velocity profiles,

$$U^+ = U^+_S E + U^{*+}_R (1 - E), \quad (4.17)$$

where E is given by an error function in the IBL, and set to 0 to recover the rough-wall profile above it,

$$E(z^+; \mu, \sigma) = \begin{cases} \dfrac{1}{2}\left[1 - \mathrm{erf}\left(\dfrac{\ln(z^+) - \mu}{\sqrt{2\sigma^2}}\right)\right], & \text{for } z < \delta_i, \\ 0, & \text{for } z \geqslant \delta_i \end{cases} \quad (4.18)$$

with the parameters modelled as

$$\mu = \ln(\delta_i^+) - \mu_0, \quad \mu_0 = 0.7 \quad \text{and} \quad \sigma = 1.0. \quad (4.19a\text{–}c)$$

The EL thickness, δ_e, can be readily derived from E. For instance, by setting a threshold at $E = 0.99$ (i.e. roughly 1 % difference between U^+ and U^+_S), an EL thickness of $\delta_e = 0.05\delta_i$ results, and a threshold at $E = 0.95$ leads to $\delta_e = 0.1\delta_i$. These are in good agreement with previous δ_e definitions based on the mean velocity or shear-stress profiles in numerical studies (Shir 1972; Rao *et al.* 1974; Rouhi *et al.* 2019).

Here, δ_i^+ is the viscous-scaled IBL thickness as determined from the 'kink' in the mean velocity or variance profile. In § 3.3, we have previously shown that as the mean flow within the IBL deviates from a canonical smooth-wall profile, δ_i determined directly from the 'kink' in the measured profile is consistently lower than $\delta_{i,log}$, which is defined as the wall-normal location where the assumed equilibrium smooth-wall mean velocity profile scaled with the local $U_{\tau 2}$ intersects the outer-layer mean velocity profile. If the mean velocity in the IBL is the same as that of a canonical smooth-wall boundary layer, then $\delta_i = \delta_{i,log}$, as in the case with all the model predictions we have made so far. From this point on, the recovering flow in the IBL is modelled by a blending velocity profile, and we must distinguish the difference between δ_i and $\delta_{i,log}$, which according to figure 7 can be approximately modelled as a constant shift when scaled by $U_{\tau 0}$:

$$\frac{\delta_{i,log} U_{\tau 0}}{\nu} = \frac{\delta_i U_{\tau 0}}{\nu} + \Delta\delta_i^+. \quad (4.20)$$

The constant shift is chosen as $\Delta\delta_i^+ = 500$ as discussed in § 3.3.

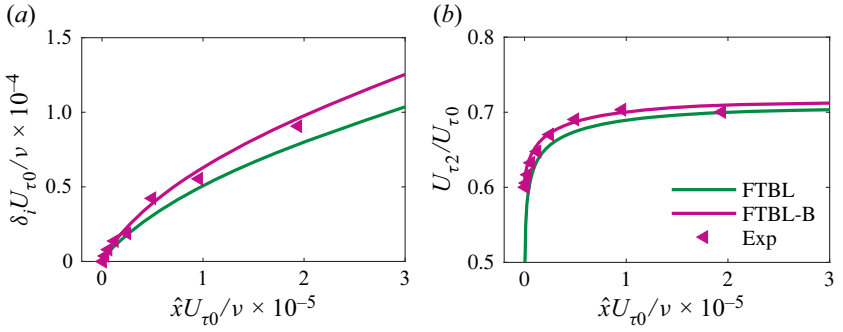

Figure 13. A comparison of the predicted (*a*) δ_i, IBL thickness; (*b*) $U_{\tau 2}$, friction velocity at the downstream surface from FTBL and FTBL-B models with experimental data. The parameters of the rough-to-smooth change are matched to case Re14ks16 with $k_{s1}U_{\tau 0}/\nu = 160$ and $Re_{\tau c0} = 16\,500$.

In summary, in the blending velocity model described above, there are three empirically determined parameters, namely $\Delta\delta_i^+$ (see § 3.3), μ_0 and σ (see Li *et al.* 2021). Here for the FTBL-B model, we use $(\Delta\delta_i^+, \mu_0, \sigma) = (500, 0.7, 1.0)$ as determined in the previous study, and compare the predictions with the results of the FTBL model in figure 13. The FTBL-B model predicts slightly higher δ_i and $U_{\tau 2}$ compared with the FTBL model, and the effect of the blending velocity profile is most pronounced in the $U_{\tau 2}$ close to the rough-to-smooth change. Overall, the FTBL-B model offers a small improvement in the agreement with experimental data (shown by the symbols in figure 13).

5. Comparison with the experimental data

Finally, the performance of the FTBL-B model is tested by comparing the model prediction with the experimentally obtained data in this section. To draw a direct comparison with the experimental results, a prediction is made for each case using the same $Re_{\tau 0}$ and k_{s0}^+ as in the experiments.

Figure 14 shows the comparison between the mean velocity profiles measured experimentally (symbols), and those predicted by the E58 model (grey solid lines) and the FTBL-B model (black solid lines). Case Re21ks16 is shown here as an example, and qualitatively similar results are observed in all other cases. Despite an obvious absence of the wake in the outer layer as well as an inner profile in the buffer region and below, the E58 model also does not capture the velocity profile in the logarithmic region close to the roughness transition (see figure 14*a*,*b*). The FTBL-B model has an improved agreement with the measured profile compared with the original one. The relative error shown in figure 14(*c*,*d*) highlights the improvement by the FTBL-B model especially in the near-wall and wake regions. We would like to note that the predictions of the original and refined models are tested against the experimental dataset acquired in this study, which has also been used to obtain the coefficients in the blending model of the mean velocity profile. For future works, a wider range of experimental data from various sources and flow conditions is necessary to further evaluate the performance of the refined model.

The performance of the E58 and FTBL-B models can be further assessed by comparing the predicted parameters. The IBL thickness δ_i is shown in figure 15. The δ_i extracted from the measured profiles are shown by symbols, while the predictions using the E58 and FTBL-B models are shown by black and coloured curves, respectively. The same legend will be adhered to in the following figures. The prediction of the FTBL-B model is close

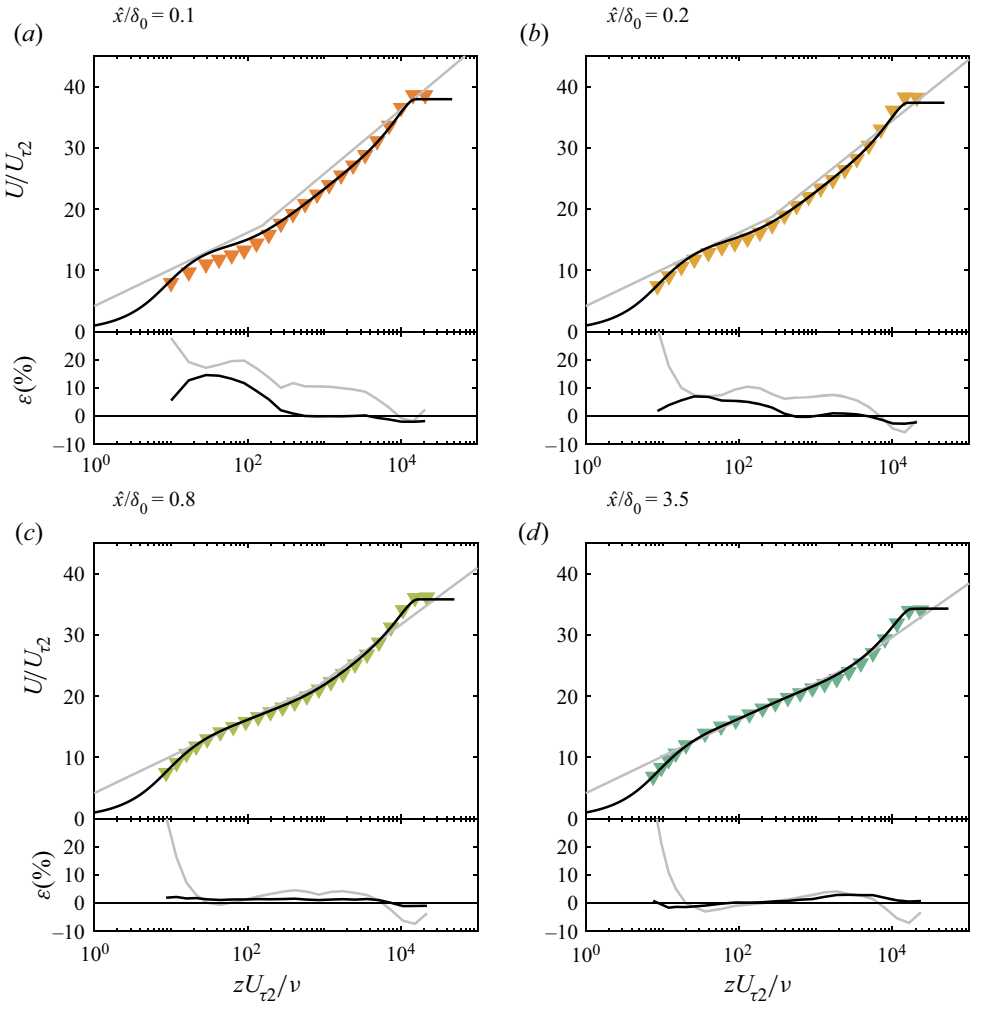

Figure 14. (*a*,*b*) Mean velocity profiles normalised by the local $U_{\tau 2}$ for case Re21ks16. The experimental data are shown by the symbols, while the thick black and grey lines represent the FTBL-B and E58 models, respectively. Panels (*c*,*d*) show the relative error in $U/U_{\tau 2}$ predicted by FTBL-B (thick black lines) and E58 (grey lines) models, with the experimental data as the baseline. Panels (*a*,*b*,*c*,*d*) are at $\hat{x}/\delta_0 = 0.1$, 0.2, 0.8 and 3.5, corresponding to $\hat{x}U_{\tau 0}/\nu = 2200$, 4400, 18 000 and 75 000, respectively.

to the results of the E58 model but now captures well the dependence on the friction Reynolds number, which was absent in Elliott's original formulation. In figure 15(*a*), both the experimental data and the FTBL-B model show that for a higher $Re_{\tau 0}$, a higher $\delta_i U_{\tau 0}/\nu$ is observed in the far field, and the FTBL-B model prediction approximates that of E58 with increasing $Re_{\tau 0}$. This is expected, because the dependence on $Re_{\tau 0}$ primarily results from the inclusion of the wake function in the FTBL-B model, and at a higher $Re_{\tau 0}$ the logarithmic region is wider and the assumptions in the E58 model are valid for a longer fetch. Similar to the prediction from the E58 model, the slight increase of δ_i with k_{s0}^+ is also reflected in the prediction from the FTBL-B model as shown in figure 15(*d*). We lack the range of k_{s0}^+ to see the trend of δ_i with k_{s0}^+ in the current experiments.

The local friction velocity $U_{\tau 2}$ on the downstream smooth wall is shown in figure 16. Similar to the previous figure, here we use coloured symbols to represent $U_{\tau 2}$ measured

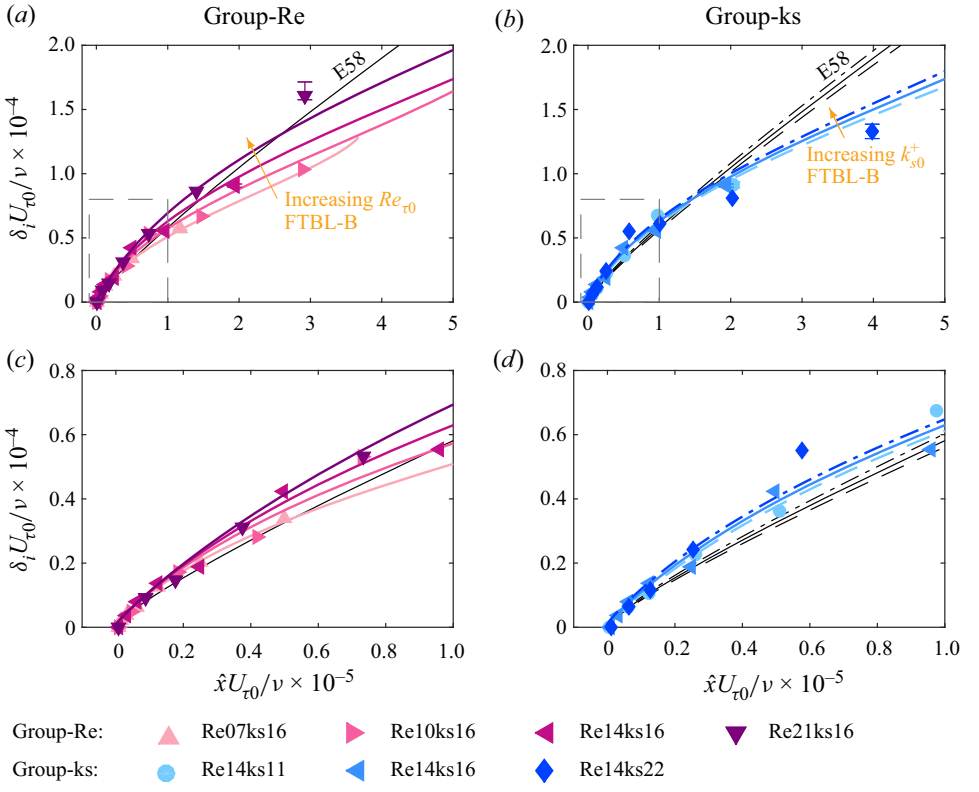

Figure 15. Profile-based IBL thickness δ_i obtained from experimental measurements (symbols) and FTBL-B model predictions (coloured lines). Symbols and colours are defined in table 1. Predictions using the E58 model are shown by the black lines; dashed, solid and dot–dashed lines correspond to $k_{s0}^+ = 111$, 160 and 230, respectively. Note that the relationship between δ_i and $\delta_{i,log}$ for the blending model is given by (4.20). The Group-Re and Group-ks cases are shown in (*a*,*b*), respectively, while (*c*,*d*) are the zoomed views of (*a*,*b*) in the vicinity of the step change. The error bar on selected data points shows the change in δ_i with a $\pm 10\,\%$ variation in the threshold used to determine δ_i from the streamwise change of the variance profile (Li *et al.* 2021).

experimentally, black and coloured curves for predictions by the E58 and FTBL-B model, respectively. Close to the roughness transition, $U_{\tau 2}$ predicted using the refined model is higher than that of the original model, leading to an improved agreement between the experimental data and prediction in the near field for both Group-Re and Group-ks. This is particularly noticeable in the zoomed views given in figure 16(*c*,*d*). This improvement is mainly contributed by the refinement of $\Delta\delta_i^+$ very close to the step change (where the fetch is a few hundred viscous units), while the non-equilibrium effect described by μ_0 is the predominant factor in the intermediate range (where the fetch is $\sim O(10^4)$ viscous units). At large $\hat{x}$ in figure 16(*a*), $U_{\tau 2}$ predicted by the FTBL-B model also approaches that by the E58 model as $Re_{\tau 0}$ increases. As shown by the Group-ks results in figure 16(*b*,*d*), the effect of k_{s0}^+ on $U_{\tau 2}$ is much stronger than that on δ_i, and the decrease of $U_{\tau 2}/U_{\tau 0}$ with increasing k_{s0}^+ is clearly visible in both model predictions and experimental data.

The outer quantities, δ_{99} and $U_{\tau 1}$ are shown in figure 17. Note that although we use δ_c (the boundary layer thickness following the definition of Jones *et al.* (2001) in the refined model), here we present the results of δ_{99} interpolated from each predicted profile to allow an easier comparison with the experiments. In the E58 model, δ_{99} (or any form of the

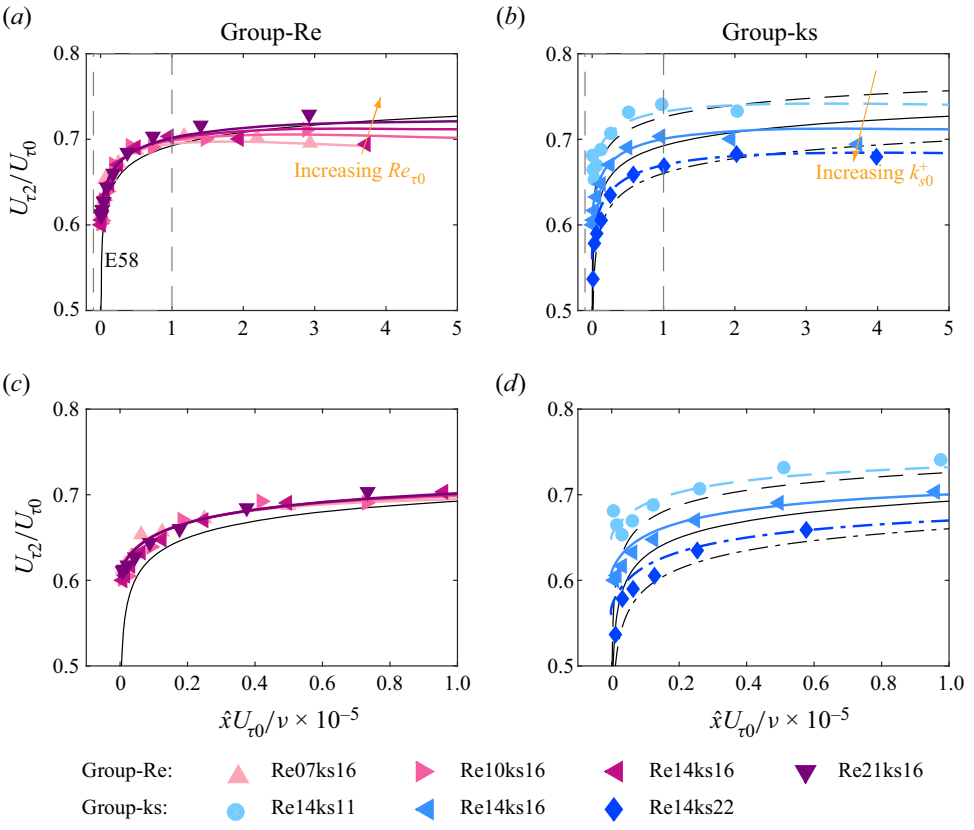

Figure 16. The friction velocity, $U_{\tau 2}$, on the downstream smooth wall obtained from experimental measurements (symbols), E58 model predictions (black lines) and FTBL-B model predictions (coloured lines). Legends are the same as in figure 15. The Group-Re and Group-ks cases are shown in (*a*,*b*), respectively, while (*c*,*d*) are the zoomed views of (*a*,*b*) in the vicinity of the step change.

boundary layer thickness) is absent and $U_{\tau 1}$ is assumed to be equal to $U_{\tau 0}$ at all streamwise locations, so here we only show the coloured lines (predictions from the FTBL-B model) in the figure to compare with the experimental results. The growth of δ_{99} becomes less aggressive after the roughness transition compared with a rough-wall turbulent boundary layer (Li *et al.* 2021). As shown in figure 17(*a*,*b*), the growth of δ_{99} is well captured by the refined model in both Group-Re and Group-ks. The outer-layer friction velocity scale $U_{\tau 1}$ is shown in figures 17(*c*) and 17(*d*). The symbols represent $U_{\tau 1}$ computed from the measured turbulence intensity profiles with an assumed outer-layer similarity, following the method detailed in Li *et al.* (2021). Despite the good agreement between the predicted and measured δ_{99}, the experimentally observed decrease of $U_{\tau 1}$ with an increasing $\hat{x}$ is much faster than the predicted trend from the model. For instance, at $\hat{x}U_{\tau 0}/\nu = 1.5 \times 10^5$, the measured $U_{\tau 1}$ for case Re21ks16 has decreased by 3 % compared with its upstream value while the prediction shows less than 1 % drop. For a given δ_c, the measured $U_{\tau 1}$ appears to be lower than the results computed using the outer-layer relationship (4.4). We speculate that a high rough-wall $U_{\tau 1}$ cannot be sustained by the low near-wall production when the flow in the IBL is being replaced by smooth-wall structures. In future work, a new relationship other than (4.4) may be required to account for the decay of $U_{\tau 1}$ in the streamwise direction.

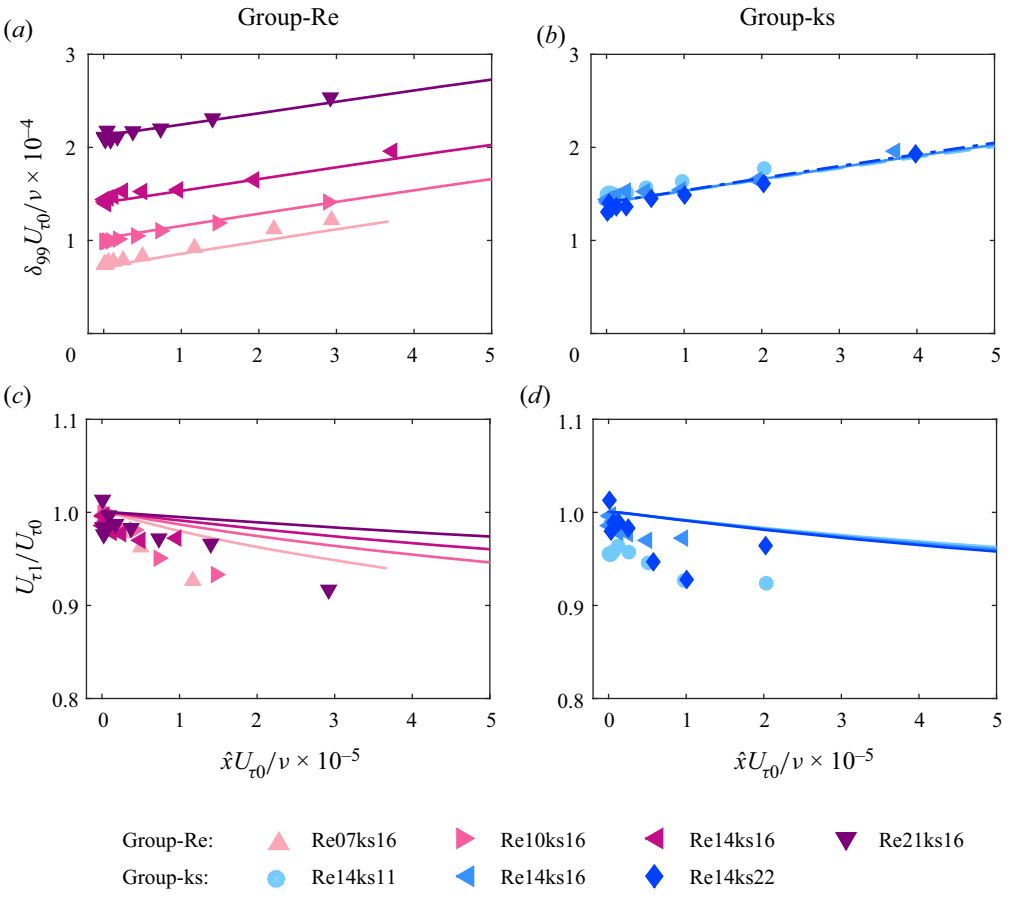

Figure 17. Comparison of δ_{99} and $U_{\tau1}$ obtained from experimental data and predicted by the E58 and FTBL-B models. The experimental data are shown by the corresponding symbols while the model predictions are shown by lines.

6. Conclusions

In this study, we numerically restate Elliott's (1958) classical model of the mean velocity evolution in the streamwise direction after a roughness transition, and provide further refinements of the model by considering more physically realistic assumptions for a developing turbulent boundary layer. The major findings are summarised below.

On the basis of Elliott's original model, we consider several refinements, including adding a wake function to the logarithmic velocity profile, modelling the decay of the shear stress when δ_i exceeds the constant-stress layer, modelling the streamwise evolution of the outer layer with two additional governing equations, and replacing the inner log-law profile with the blending model to account for the non-equilibrium behaviour in the IBL. After implementing these refinements, an improved agreement between the model prediction and the experimental data is observed. So far, the FTBL-B model has only been tested against the present experimental dataset. Comparison with a wider range of datasets from various sources is required in future works.

Compared with the original E58 model which is intended for a deep surface layer, the refinements developed here make the model more suitable for a spatially developing turbulent boundary layer with a finite thickness. Some refinements, including the

consideration of a wake profile, the shear stress profile and the streamwise growth of the entire boundary layer thickness, can also be applied to smooth-to-rough transitions. The blending mean velocity profile has only been tested in the rough-to-smooth case, although in the future the validity of the concept can be explored in other roughness heterogeneity scenarios.

Supplementary material. Supplementary material is available at https://doi.org/10.1017/jfm.2022.731.

Acknowledgements. This research was supported under the Australian Research Council's Discovery and Linkage Projects funding scheme (projects DP160103619 and LP190101134).

Declaration of interests. The authors report no conflict of interest.

Author ORCIDs.
Mogeng Li https://orcid.org/0000-0002-9875-6468;
Charitha M. de Silva https://orcid.org/0000-0001-9517-4318;
Daniel Chung https://orcid.org/0000-0003-3732-364X;
Ivan Marusic https://orcid.org/0000-0003-2700-8435.

Appendix A. Friction velocity ratio $U_{\tau 2}/U_{\tau 0}$ far downstream of a rough-to-smooth change in a finite-thickness turbulent boundary layer

This appendix details a theoretical analysis of the aforementioned far-field behaviour which is not captured by Elliott's model. We continue using $U_{\tau 2}$ and $U_{\tau 0}$ to denote the friction velocities of the smooth-wall and rough-wall boundary layers, respectively, although in the following derivation we assume that these two boundary layers are in quasiequilibrium with the local surface condition (rather than in the recovering state as discussed above). The boundary layer thicknesses on the smooth wall and rough wall are denoted by δ and δ_0, respectively. Note that δ is larger than δ_0 due to the growth of the boundary layer downstream of the step change. The two boundary layers are assumed to share the same wake function $\mathcal{W}(z/\delta)$ (or $\mathcal{W}(z/\delta_0)$ on the rough wall). Here U_∞^+ for a canonical smooth-wall turbulent boundary layer can be expressed as

$$\frac{U_\infty}{U_{\tau 2}} = \frac{1}{\kappa}\ln\left(\frac{\delta U_{\tau 2}}{\nu}\right) + B + \frac{2\Pi}{\kappa}\mathcal{W}(1), \tag{A1}$$

while its rough-wall counterpart is

$$\frac{U_\infty}{U_{\tau 0}} = \frac{1}{\kappa}\ln\left(\frac{\delta_0 U_{\tau 0}}{\nu}\right) + A'_{FR} - \frac{1}{\kappa}\ln(k_{s0}^+) + \frac{2\Pi}{\kappa}\mathcal{W}(1). \tag{A2}$$

Therefore, the friction velocity ratio is

$$\begin{aligned}\frac{U_{\tau 2}}{U_{\tau 0}} &= \frac{\dfrac{1}{\kappa}\ln\left(\dfrac{\delta_0 U_{\tau 0}}{\nu}\right) + A'_{FR} - \dfrac{1}{\kappa}\ln(k_{s0}^+) + \dfrac{2\Pi}{\kappa}\mathcal{W}(1)}{\dfrac{1}{\kappa}\ln\left(\dfrac{\delta U_{\tau 2}}{\nu}\right) + B + \dfrac{2\Pi}{\kappa}\mathcal{W}(1)} \\ &= \frac{\dfrac{1}{\kappa}\ln\left(\dfrac{\delta_0 U_{\tau 0}}{\nu}\right) + A'_{FR} - \dfrac{1}{\kappa}\ln(k_{s0}^+) + \dfrac{2\Pi}{\kappa}\mathcal{W}(1)}{\dfrac{1}{\kappa}\ln\left(\dfrac{\delta_0 U_{\tau 0}}{\nu}\right) + \dfrac{1}{\kappa}\ln\left(\dfrac{U_{\tau 2}}{U_{\tau 0}}\right) + \dfrac{1}{\kappa}\ln\left(\dfrac{\delta}{\delta_0}\right) + B + \dfrac{2\Pi}{\kappa}\mathcal{W}(1)}.\end{aligned} \tag{A3}$$

For Group-Re cases, k_{s0}^{+} is held constant. Therefore, we can define two constants

$$C_0 = A'_{FR} - \frac{1}{\kappa}\ln(k_{s0}^{+}) + \frac{2\Pi}{\kappa}\mathcal{W}(1), \tag{A4}$$

$$C = B + \frac{2\Pi}{\kappa}\mathcal{W}(1), \tag{A5}$$

and two non-dimensional quantities

$$U_{\tau 2}^{*} = \frac{U_{\tau 2}}{U_{\tau 0}}, \tag{A6}$$

$$\delta^{*} = \frac{\delta}{\delta_0}. \tag{A7}$$

Also note that $Re_{\tau 0} \equiv U_{\tau 0}\delta_0/\nu$, thus (A3) can be rearranged to

$$F(U_{\tau 2}^{*}, Re_{\tau 0}, \delta^{*}) = U_{\tau 2}^{*}\left(\frac{1}{\kappa}\ln Re_{\tau 0} + \frac{1}{\kappa}\ln U_{\tau 2}^{*} + \frac{1}{\kappa}\ln\delta^{*} + C\right) - \frac{1}{\kappa}\ln Re_{\tau 0} - C_0 = 0. \tag{A8}$$

For a prescribed δ^{*} (which is approximately equivalent to a given fetch), the dependence of $U_{\tau 2}^{*}$ on $Re_{\tau 0}$ can be studied using the chain rule. Equation (A8) is differentiated with regard to $Re_{\tau 0}$ while δ^{*} is held constant:

$$0 = \frac{\partial F}{\partial Re_{\tau 0}} + \frac{\partial F}{\partial U_{\tau 2}^{*}}\frac{\mathrm{d}U_{\tau 2}^{*}}{\mathrm{d}Re_{\tau 0}}. \tag{A9}$$

The derivative is solved as

$$\frac{\mathrm{d}U_{\tau 2}^{*}}{\mathrm{d}Re_{\tau 0}} = \frac{\dfrac{1}{\kappa Re_{\tau 0}}(1 - U_{\tau 2}^{*})}{\dfrac{1}{\kappa}\ln Re_{\tau 0} + \dfrac{1}{\kappa}\ln U_{\tau 2}^{*} + \dfrac{1}{\kappa}\ln\delta^{*} + C}, \tag{A10}$$

which is positive as $U_{\tau 2}^{*} \lesssim 1$. This indicates that $U_{\tau 2}^{*}$ increases with $Re_{\tau 0}$ in the far field, in good agreement with the measurements shown in figure 5(*a*).

The dependence of $U_{\tau 2}^{*}$ on δ^{*} for a constant $Re_{\tau 0}$ can be obtained via a similar approach. The derivative is found as

$$\frac{\mathrm{d}U_{\tau 2}^{*}}{\mathrm{d}\delta^{*}} = \frac{-\dfrac{U_{\tau 2}^{*}}{\kappa\delta^{*}}}{\dfrac{1}{\kappa}\ln Re_{\tau 0} + \dfrac{1}{\kappa}\ln U_{\tau 2}^{*} + \dfrac{1}{\kappa}\ln\delta^{*} + C}, \tag{A11}$$

indicating a decreasing trend in $U_{\tau 2}^{*}$ as δ^{*} increases. This agrees with the observation that in the far field, $U_{\tau 2}^{*}$ decreases with $\hat{x}U_{\tau 0}/\nu$ in each case in figure 5(*a*).

Appendix B. Modified Musker mean velocity profile

We adopt the expression of the inner mean velocity profile of a smooth-wall turbulent boundary layer proposed by Chauhan *et al.* (2009). The Musker inner profile is given by

$$U^+_{inner} = \frac{1}{\kappa}\ln\left(\frac{z^+-a}{-a}\right) + \frac{R^2}{a(4\alpha-a)}\left[-\frac{a}{R}\frac{\sqrt{(z^+-\alpha)^2+\beta^2}}{z^+-a} + \frac{\alpha}{\beta}(4\alpha+5a)\left(\arctan\left(\frac{z^+-\alpha}{\beta}\right)+\arctan\left(\frac{\alpha}{\beta}\right)\right)\right], \tag{B1}$$

with $\alpha = (-1/\kappa - a)/2$, $\beta = \sqrt{-2a\alpha-\alpha^2}$ and $R = \sqrt{\alpha^2+\beta^2}$. For consistency with the logarithmic law constants $\kappa = 0.384$ and $B = 4.17$, a is chosen as -10.3061. To account for the undershoot for the indicator function $z^+(\mathrm{d}U^+/\mathrm{d}z^+)$ at around $z^+ \approx 50$, an exponential term is added to the original expression (Monkewitz, Chauhan & Nagib 2007):

$$U^+_{inner}(modified) = U^+_{inner} + \frac{\exp[-\ln^2(z^+/30)]}{2.85}. \tag{B2}$$

Appendix C. Initial condition

The initial condition is chosen as $\delta_i(0) = \max(z_{01}, z_{02})$. This is the smallest value δ_i can take without resulting in a negative U or $U_{\tau 2}$. The initial value of $U_{\tau 2}$ is determined subsequently via (2.4). It is possible to start the evolution with a higher δ_i at $\hat{x} = 0$ and a few examples are shown in figure 18(*a*,*b*). This figure shows the evolution of $\delta_i U_{\tau 1}/\nu$ as a function of $\hat{x}U_{\tau 1}/\nu$, computed using the numerical implementation of Elliott's model as described in (3.3)–(3.1*a*,*b*). A piecewise log profile as depicted in figure 2(*b*) is used in the calculation.

Rough-to-smooth and smooth-to-rough cases are shown in figures 18(*a*) and 18(*b*), respectively. The line colours, red, orange, green and blue correspond to increasing $\delta_i(0)$. A higher $\delta_i(0)$ will lead to a higher δ_i farther downstream. If we choose the red line with $\delta_i(0) = \max(z_{01}, z_{02})$ from figure 18(*a*,*b*) as the baseline case, and shift the other three lines downstream until the first point in each line falls on top of the red line, we can see an almost perfect collapse for the remaining part of the curves. This scenario is presented in figure 18(*c*,*d*). In other words, using a different starting point of $\delta_i(0)$ does not change the shape of the predicted δ_i versus $\hat{x}$ curve: it is essentially equivalent to displacing the curve in x by a certain amount. To demonstrate this analytically, we consider two different initial values $\delta_{i1}(0)$ and $\delta_{i2}(0)$ and compute the corresponding fetch $\hat{x}_1$ and $\hat{x}_2$ following (3.3):

$$\begin{aligned}\hat{x}_2(\delta_i) &= \int_{\delta_{i2}(0)}^{\delta_i}\frac{\rho}{\Delta\tau(\xi)}G_2'(\xi)\,\mathrm{d}\xi - \int_{\delta_{i2}(0)}^{\delta_i}\frac{\rho U_i(\xi)}{\Delta\tau(\xi)}G_1'(\xi)\,\mathrm{d}\xi \\ &= \left(\int_{\delta_{i2}(0)}^{\delta_{i1}(0)} + \int_{\delta_{i1}(0)}^{\delta_i}\right)\frac{\rho}{\Delta\tau(\xi)}G_2'(\xi)\,\mathrm{d}\xi - \left(\int_{\delta_{i2}(0)}^{\delta_{i1}(0)} + \int_{\delta_{i1}(0)}^{\delta_i}\right)\frac{\rho U_i(\xi)}{\Delta\tau(\xi)}G_1'(\xi)\,\mathrm{d}\xi \\ &= \int_{\delta_{i2}(0)}^{\delta_{i1}(0)}\frac{\rho}{\Delta\tau(\xi)}\left[G_2'(\xi) - U_i(\xi)G_1'(\xi)\right]\mathrm{d}\xi + \hat{x}_1(\delta_i).\end{aligned} \tag{C1}$$

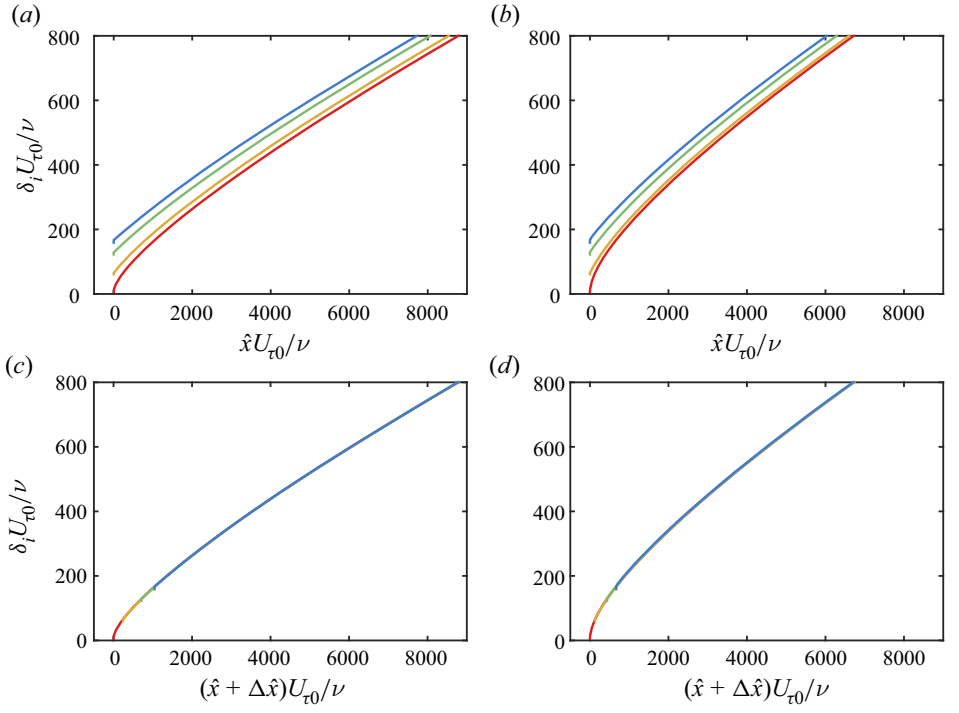

Figure 18. Predicted IBL thicknesses δ_i using (2.3) and (3.3) for (*a*) rough-to-smooth and (*b*) smooth-to-rough cases. Panels (*c*,*d*) show the same data as in (*a*,*b*) but with the abscissa shifted by $\Delta\hat{x}$ (see (C2) for the analytical expression) for each curve. Line colours red, orange, green and blue correspond to $\delta_i(0)/\max(z_{01}, z_{02}) = 1$, 10, 20 and 26, respectively. Note that $\delta_i(0)/\max(z_{01}, z_{02}) = 26$ is approximately $\delta_i(0)/\max(k_{s1}, k_{s2}) = 1$. For both rough-to-smooth and smooth-to-rough cases, $\max(k_{s1}, k_{s2})U_{\tau 1}/\nu = 160$.

Therefore, $\Delta\hat{x}$, the shift in $\hat{x}$ required for the two predictions with different initial conditions to match can be expressed as

$$\Delta\hat{x} = \hat{x}_2(\delta_i) - \hat{x}_1(\delta_i) = \int_{\delta_{i2}(0)}^{\delta_{i1}(0)} \frac{\rho}{\Delta\tau(\xi)}\left[G_2'(\xi) - U_i(\xi)G_1'(\xi)\right]\mathrm{d}\xi. \tag{C2}$$

With $\delta_{i1}(0)$ and $\delta_{i2}(0)$ as the upper and lower limits of the integral being constants, it is apparent that $\Delta\hat{x}$ is also a constant (for any value of δ_i, and therefore for any $\hat{x}$ location).

Appendix D. Model variations

The predicted results with refinements detailed in §§ 4.1–4.3 are summarised in figure 19. We compare the predicted $\delta_i U_{\tau 0}/\nu$ and $U_{\tau 2}/U_{\tau 0}$ of the original E58 model with those after accumulatively introducing each refinement. The wake refinement (§ 4.1) is labelled as 'Π', the growing outer layer (detailed in § 4.2) is labelled as '$\delta_c(\hat{x})$' and the shear-stress correction (§ 4.3) is labelled as 'τ'. For the rough-to-smooth case shown in figure 19(*a*,*c*), including a wake function ('Π') leads to a lower $\delta_i U_{\tau 0}/\nu$ and a higher $U_{\tau 2}/U_{\tau 0}$. After introducing the growth of $\delta_c(\hat{x})$ ('$\Pi + \delta_c(\hat{x})$'), this effect is cancelled in the near field ($\hat{x}U_{\tau 0}/\nu \lesssim 1.5 \times 10^5$), but the predicted $\delta_i U_{\tau 0}/\nu$ continues to grow rapidly and overshoots the result from the E58 model. Finally, after incorporating the shear-stress correction ('$\Pi + \delta_c(\hat{x}) + \tau$', equivalent to FTBL), the predicted $\delta_i U_{\tau 0}/\nu$ follows a similar trend as that of case Π, while $U_{\tau 2}/U_{\tau 0}$ is lower than that of E58. For the

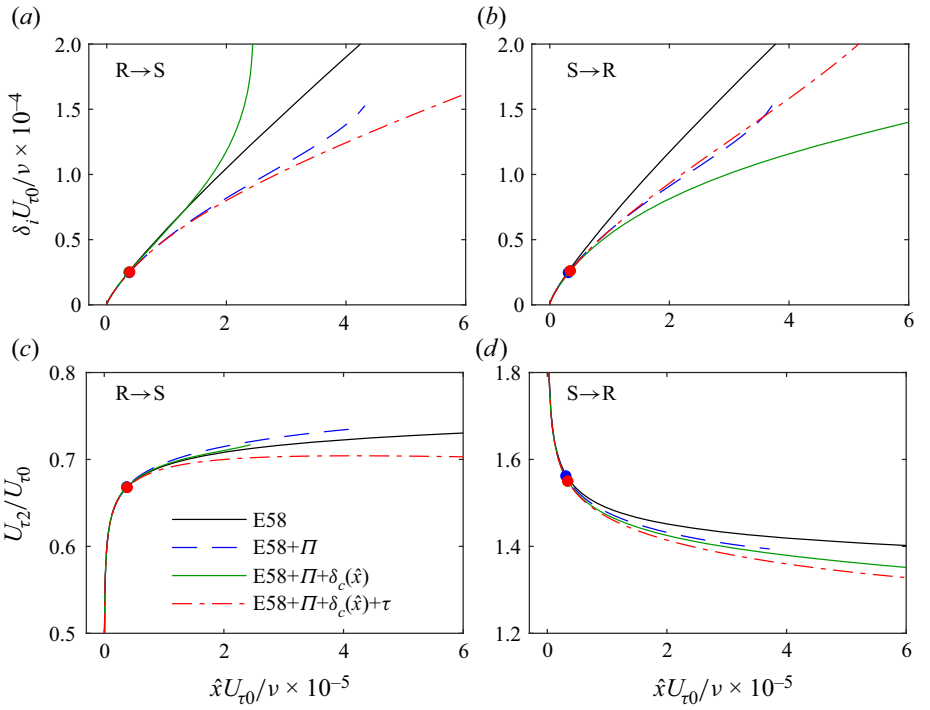

Figure 19. Comparison of the predictions from Elliott's original model ('E58' as in the legend), the refined model with the a wake function ('Π'), with both wake and a δ_c that evolves in the streamwise direction ('$\Pi + \delta_c(\hat{x})$'), and finally with shear-stress correction on top of both wake and growing δ_c refinements ('$\Pi + \delta_c(\hat{x}) + \tau$'). Panels (*a*,*c*) are for the rough-to-smooth case and (*b*,*d*) are for the smooth-to-rough case. Panels (*a*,*b*) are the IBL thickness and (*c*,*d*) are the ratio between the downstream and upstream friction velocity. The coloured dot on each curve marks the location where $\delta_i = 0.15\delta_c$, representing the onset of the wake region. For both rough-to-smooth and smooth-to-rough cases, $\max(k_{s1}, k_{s2})U_{\tau 0}/\nu = 160$ and $Re_{\tau c} = 16\,500$. The flow conditions of the rough-to-smooth case are matched to case Re14ks16.

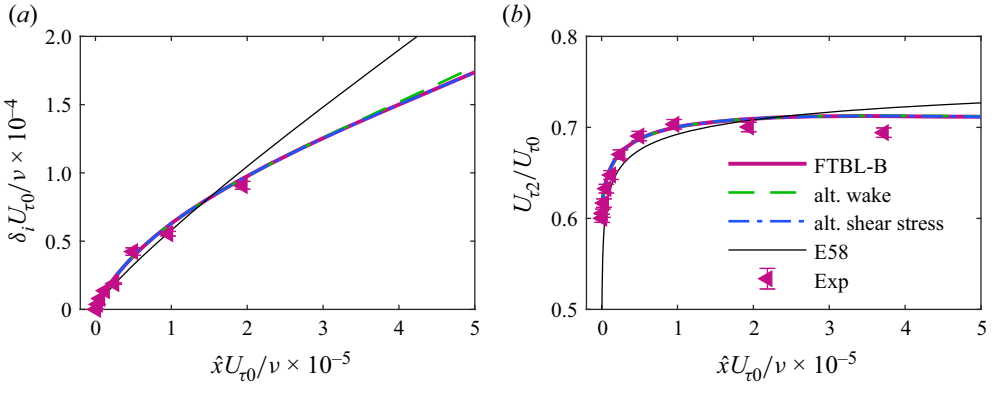

Figure 20. Predictions of the E58 and FTBL models, and the modified FTBL model with alternative wake and shear-stress profiles. Panel (*a*) is the IBL thickness and (*b*) is the friction velocity ratio. We obtained δ_i by thresholding the streamwise variation in the variance profiles (Li *et al.* 2021), and the error bars in (*a*) show the change in δ_i when this threshold is varied by $\pm 10\,\%$. The error bars in (*b*) are the estimated repeatability of the present OFI measurement (Li *et al.* 2019).

smooth-to-rough case in figure 19(*b*,*d*), 'Π' refinement lowers both $\delta_i U_{\tau 0}/\nu$ and $U_{\tau 2}/U_{\tau 0}$, and the combination '$\Pi + \delta_c(\hat{x})$' makes $\delta_i U_{\tau 0}/\nu$ even lower. However, by including the shear-stress correction ('$\Pi + \delta_c(\hat{x}) + \tau$'), $\delta_i U_{\tau 0}/\nu$ is brought back to a similar trend as that of 'Π'. To summarise, after incorporating the refinements detailed in §§ 4.1–4.3, the predicted $\delta_i U_{\tau 0}/\nu$ and $U_{\tau 2}/U_{\tau 0}$ are found to be lower than that of E58 in both rough-to-smooth and smooth-to-rough cases.

Figure 20 shows the predictions of the FTBL model with alternative choices of the wake and shear-stress profiles. Here, we substitute (4.1) with a sine-squared wake function (Coles 1956) with cubic correction to ensure a zero velocity gradient at the edge of the boundary layer, and (4.8) with a simple cosine function as $\tau^+ = [\cos(\pi\eta) + 1]/2$. These different choices of the exact forms have little influence on the model predictions.

References

Abkar, M. & Porté-Agel, F. 2012 A new boundary condition for large-eddy simulation of boundary-layer flow over surface roughness transitions. *J. Turbul.* **13**, N23.

Antonia, R.A. & Luxton, R.E. 1971 The response of a turbulent boundary layer to a step change in surface roughness. Part 1. Smooth to rough. *J. Fluid Mech.* **48**, 721–761.

Antonia, R.A. & Luxton, R.E. 1972 The response of a turbulent boundary layer to a step change in surface roughness. Part 2. Rough-to-smooth. *J. Fluid Mech.* **53**, 737–757.

Atkinson, K.E. 1989 *An Introduction to Numerical Analysis*. John Wiley & Sons.

Baars, W.J., Squire, D.T., Talluru, K.M., Abbassi, M.R., Hutchins, N. & Marusic, I. 2016 Wall-drag measurements of smooth-and rough-wall turbulent boundary layers using a floating element. *Exp. Fluids* **57** (5), 90.

Bou-Zeid, E., Anderson, W., Katul, G.G. & Mahrt, L. 2020 The persistent challenge of surface heterogeneity in boundary-layer meteorology: a review. *Boundary-Layer Meteorol.* **177** (2), 227–245.

Bou-Zeid, E., Meneveau, C. & Parlange, M.B. 2004 Large-eddy simulation of neutral atmospheric boundary layer flow over heterogeneous surfaces: blending height and effective surface roughness. *Water Resour. Res.* **40**, W02505.

Chamorro, L.P. & Porté-Agel, F. 2009 Velocity and surface shear stress distributions behind a rough-to-smooth surface transition: a simple new model. *Boundary-Layer Meteorol.* **130**, 29–41.

Chauhan, K.A., Monkewitz, P.A. & Nagib, H.M. 2009 Criteria for assessing experiments in zero pressure gradient boundary layers. *Fluid Dyn. Res.* **41**, 021404.

Coles, D. 1956 The law of the wake in the turbulent boundary layer. *J. Fluid Mech.* **1** (2), 191–226.

Elliott, W.P. 1958 The growth of the atmospheric internal boundary layer. *Trans. Am. Geophys. Union* **39**, 1048–1054.

Garratt, J.R. 1990 The internal boundary layer – a review. *Boundary-Layer Meteorol.* **50**, 171–203.

Ghaisas, N.S. 2020 A predictive analytical model for surface shear stresses and velocity profiles behind a surface roughness jump. *Boundary-Layer Meteorol.* **176** (3), 349–368.

Ismail, U., Zaki, T.A. & Durbin, P.A. 2018 Simulations of rib-roughened rough-to-smooth turbulent channel flows. *J. Fluid Mech.* **843**, 419–449.

Jackson, N.A. 1976 The propagation of modified flow downstream of a change in roughness. *Q. J. R. Meteorol. Soc.* **102** (434), 924–933.

Jones, M.B., Marusic, I. & Perry, A.E. 2001 Evolution and structure of sink-flow turbulent boundary layers. *J. Fluid Mech.* **428**, 1–27.

Li, M., de Silva, C.M., Baidya, R., Rouhi, A., Chung, D., Marusic, I. & Hutchins, N. 2019 Recovery of the wall-shear stress to equilibrium flow conditions after a rough-to-smooth step-change in turbulent boundary layers. *J. Fluid Mech.* **872**, 472–491.

Li, M., de Silva, C.M., Chung, D., Pullin, D.I., Marusic, I. & Hutchins, N. 2021 Experimental study of a turbulent boundary layer with a rough-to-smooth change in surface conditions at high Reynolds numbers. *J. Fluid Mech.* **923**, A18.

Marusic, I., Chauhan, K.A., Kulandaivelu, V. & Hutchins, N. 2015 Evolution of zero-pressure-gradient boundary layers from different tripping conditions. *J. Fluid Mech.* **783**, 379–411.

Miyake, M. 1965 *Transformation of the Atmospheric Boundary Layer Over Inhomogeneous Surfaces*. Department of Atmospheric Sciences, University of Washington.

Monkewitz, P.A., Chauhan, K.A. & Nagib, H.M. 2007 Self-consistent high-Reynolds-number asymptotics for zero-pressure-gradient turbulent boundary layers. *Phys. Fluids* **19** (11), 115101.

MORRILL-WINTER, C., SQUIRE, D.T., KLEWICKI, J.C., HUTCHINS, N., SCHULTZ, M.P. & MARUSIC, I. 2017 Reynolds number and roughness effects on turbulent stresses in sandpaper roughness boundary layers. *Phys. Rev. Fluids* **2**, 054608.

NIKURADSE, J. 1950 Laws of flow in rough pipes. *NACA Tech. Memo.* 1292.

PANOFSKY, H.A. & DUTTON, J.A. 1984 *Atmospheric Turbulence*, p. 397. Wiley.

PANOFSKY, H.A. & TOWNSEND, A.A. 1964 Change of terrain roughness and the wind profile. *Q. J. R. Meteorol. Soc.* **90** (384), 147–155.

PETERSON, E.W. 1969 Modification of mean flow and turbulent energy by a change in surface roughness under conditions of neutral stability. *Q. J. R. Meteorol. Soc.* **95** (405), 561–575.

RAO, K.S., WYNGAARD, J.C. & COTÉ, O.R. 1974 The structure of the two-dimensional internal boundary layer over a sudden change of surface roughness. *J. Atmos. Sci.* **31**, 738–746.

ROUHI, A., CHUNG, D. & HUTCHINS, N. 2019 Direct numerical simulation of open channel flow over smooth-to-rough and rough-to-smooth step changes. *J. Fluid Mech.* **866**, 450–486.

SAVELYEV, S.A. & TAYLOR, P.A. 2001 Notes on an internal boundary-layer height formula. *Boundary-Layer Meteorol.* **101** (2), 293–301.

SAVELYEV, S.A. & TAYLOR, P.A. 2005 Internal boundary layers. I. Height formulae for neutral and diabatic flows. *Boundary-Layer Meteorol.* **115**, 1–25.

SCHLATTER, P. & ÖRLÜ, R. 2010 Assessment of direct numerical simulation data of turbulent boundary layers. *J. Fluid Mech.* **659** (1), 116–126.

SHIR, C.C. 1972 A numerical computation of air flow over a sudden change of surface roughness. *J. Atmos. Sci.* **29** (2), 304–310.

SRIDHAR, A. 2018 Large-eddy simulation of turbulent boundary layers with spatially varying roughness. PhD thesis, California Institute of Technology.

TENNEKES, H. & LUMLEY, J.L. 1972 *A First Course in Turbulence*. MIT Press.

TOWNSEND, A.A. 1965*a* The response of a turbulent boundary layer to abrupt changes in surface conditions. *J. Fluid Mech.* **22** (4), 799–822.

TOWNSEND, A.A. 1965*b* Self-preserving flow inside a turbulent boundary layer. *J. Fluid Mech.* **22** (4), 773–797.

TOWNSEND, A.A. 1966 The flow in a turbulent boundary layer after a change in surface roughness. *J. Fluid Mech.* **26** (2), 255–266.

VAN BUREN, T., FLORYAN, D., DING, L., HELLSTRÖM, L.H.O. & SMITS, A.J. 2020 Turbulent pipe flow response to a step change in surface roughness. *J. Fluid Mech.* **904**, A38.

WOOD, D.H. 1982 Internal boundary layer growth following a step change in surface roughness. *Boundary-Layer Meteorol.* **22** (2), 241–244.

YANG, X.I.A. 2016 On the mean flow behaviour in the presence of regional-scale surface roughness heterogeneity. *Boundary-Layer Meteorol.* **161** (1), 127–143.